Journal Pre-proof

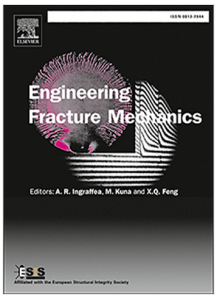

Cohesive phase-field fracture with an explicit strength surface: An eigenstrain-based return-mapping formulation

Tim Hageman

PII: S0013-7944(26)00454-6
DOI: https://doi.org/10.1016/j.engfracmech.2026.112292
Reference: EFM 112292

To appear in: *Engineering Fracture Mechanics*

Received date : 20 March 2026
Revised date : 30 April 2026
Accepted date : 18 May 2026

Please cite this article as: T. Hageman, Cohesive phase-field fracture with an explicit strength surface: An eigenstrain-based return-mapping formulation. *Engineering Fracture Mechanics* (2026), doi: https://doi.org/10.1016/j.engfracmech.2026.112292.

Highlights

Cohesive phase-field fracture with an explicit strength surface: an eigenstrain-based return-mapping formulation

Tim Hageman

- Cohesive phase-field fracture with an explicit, tuneable strength surface.
- Eigenstrains are updated by local return mapping at integration points.
- Consistent tangents for smooth and non-smooth strength criteria are derived.
- Formulation is implemented in a standard finite-element framework.
- Benchmark cases show mesh-independence and phase-field length scale independence.

Cohesive phase-field fracture with an explicit strength surface: an eigenstrain-based return-mapping formulation

Tim Hageman[a,*]

[a]*Department of Engineering Science, University of Oxford, Oxford OX1 3PJ, UK*

Abstract

Standard phase-field fracture methods are rooted in brittle fracture theory and therefore do not inherently prescribe a material strength for crack nucleation, while also struggling to capture cohesive fracture behaviour. Recent eigenstrain-based formulations overcome both limitations by introducing fracture eigenstrains that decouple the strength surface from the fracture energy, but their implementation has so far relied on direct energy-minimization frameworks rather than standard finite-element procedures. In this work, we exploit the fact that the eigenstrains require no spatial gradients and reformulate the eigenstrain evolution as a local constitutive model, analogous to those used in plasticity, that is resolved at each integration point. As a result, the cohesive phase-field requires no additional global degrees of freedom beyond those of a standard phase-field formulation and can be readily integrated into existing finite-element codes. Two strength criteria are considered: a non-smooth criterion with independent tensile and shear strengths, and a smooth Drucker-Prager-like criterion that captures pressure-dependent strengthening under compression. Consistent tangent operators are derived for both criteria, ensuring robust convergence of the global Newton-Raphson solver. The framework is validated against three benchmark problems: a plate with a hole under tension and compression, a single-edge notched plate under shear, and a notched plate under dynamic loading. The results demonstrate mesh-independent and phase-field length-scale-independent behaviour, confirm that the fracture energy governs the transition between brittle and cohesive regimes, and show that complex phenomena such as crack branching under dynamic loading are naturally captured. All source codes are openly available.

Keywords: Cohesive fracture, phase-field, eigenstrains, crack nucleation, finite element method

*Corresponding author
Email address: tim.hageman@eng.ox.ac.uk (Tim Hageman)

Nomenclature

$\mathbf{b}$	Body forces	c	Damping coefficient
$d(\phi)$	Degradation function	$\boldsymbol{D}_{\mathrm{tan}}$	Consistent tangent stiffness
E	Young's modulus	f_{s}	Shear strength
f_{t}	Tensile strength	F_{d}	Degradable strength potential
F_{i}	Non-degradable strength potential	$\boldsymbol{G}$, $\boldsymbol{G}_i$	Eigenstrain directions
G_{c}	Fracture energy release rate	$\boldsymbol{I}$	Identity matrix
K	Bulk modulus	ℓ	Phase-field length scale
$\boldsymbol{L}$	Strain–displacement operator	$\boldsymbol{N}_{\mathrm{u}}$, $\mathbf{N}_{\phi}$	Shape functions
$\mathbf{u}$	Displacement	$\gamma(\phi)$	Phase-field distribution function
$\boldsymbol{\varepsilon}$	Total strain	$\boldsymbol{\varepsilon}_{\mathrm{el}}$	Elastic strain
$\varepsilon_{\mathrm{ref}}$	Reference strain (DP criterion)	$\boldsymbol{\eta}$	Fracture eigenstrain
κ	Residual strength parameter	κ_{t}	Residual stiffness parameter
λ, λ_i	Eigenstrain multipliers	μ	Shear modulus
ν	Poisson's ratio	ρ	Density
$\boldsymbol{\sigma}$	Cauchy stress	$\boldsymbol{\tau}$	External traction
ϕ	Phase-field parameter	Ψ	Total energy
Ω	Domain	Γ_{c}	Crack surface
$\mathcal{F}$	Crack driving force (history)	$\mathrm{tr}(\cdot)$	Trace operator
$\mathrm{dev}(\cdot)$	Deviatoric operator	$\|\cdot\|$	L_2 norm
$\dot{(\cdot)}$, $\ddot{(\cdot)}$	First, second time derivative	$\langle\cdot\rangle^{\pm}$	Macaulay brackets

1. Introduction

Over the last decades, the phase-field method has become one of the most popular methods to model fracture propagation [1, 2]. Fractures are described through a partial-differential equation rather than by explicitly inserting new fracture faces, making integration within existing finite element software straightforward [3–5]. As a result, this method allows for arbitrary fracture paths, crack branching, and merging without special considerations of these features [6, 7]. Phase-field models have also been combined with a range of other physical phenomena, e.g., the numerous works on hydraulic fractures [8–11] and chemical degradation [12–15], where treating cracks as a diffuse interface makes implementing these additional phenomena straightforward.

The phase-field fracture method is based on Griffith's theory, prescribing the energy dissipated by propagating cracks and letting the fracture path itself follow from minimizing the total energy contained within the system. However, this origin in brittle fracture mechanics has also imposed a strong limitation [16, 17]: Griffith's theory does not capture when cracks nucleate as it does not prescribe a material strength. Instead, it solely predicts when cracks propagate and the energy dissipated during this propagation [18]. As a result, phase-field methods inherited the same issues, with crack propagation being modelled in a thermodynamically consistent manner, while crack nucleation often uses ad-hoc criteria. For instance, while the phase-field length scale is introduced as a regularization parameter, defining the distance over which the discrete crack is distributed, treating it as a material parameter

instead allows a material strength to be defined [19, 20]. Other approaches to capture this material strength that needs to be exceeded for cracks to nucleate include a series of stress-splitting schemes that split the elastic energy between a part that does, and does not, contribute to damage, thereby approximating strength surfaces [21–25].

A second limitation of standard phase-field methods is the difficulty to capture ductile behaviour, stemming again from the method's basis in brittle fracture mechanics. While the degradation function can be calibrated to match the unloading behaviour expected [26, 27], this calibration is done through uni-axial tension cases, and extending this behaviour to multi-axial loading is often not possible [28]. Furthermore, the damage functions do not include any fracture energy. As a result, calibration becomes material-specific, limiting application of the same models to a range of materials. Similarly, cohesive behaviour can be approximated based on the choice of phase-field distribution function [29], but this turns the choice of how to distribute the fracture energy over a finite region into a material modelling choice rather than a mathematical concept. While this limitation can be overcome by explicitly adding cohesive forces based on the displacement discontinuity, this adds extra complexity, requiring the displacement jump to be defined throughout the domain [30, 31]. Alternatively, the phase-field method can be combined with a plasticity model, using part of the plastic energy dissipated as driving force for fractures [32–34]. However, if plasticity is only expected to occur near the crack tip, this approach is both computationally expensive, requiring a sufficiently fine mesh to resolve the plastic zone around the crack tip, and requires numerous additional constitutive modelling choices.

Recent work by Vicentini et al. [35] and Bourdin et al. [36] has started to overcome these limitations, explicitly introducing tuneable failure surfaces into phase-field formulations. By introducing fracture eigenstrains that decouple the fracture release energy from the material strength, and including an explicit threshold below which cracks cannot nucleate, their formulations are able to capture material behaviour across a range of fracture energies and material strengths without relying on tuning regularization parameters or damage functions. However, while these works provide a thorough mathematical basis, their implementations solve for the eigenstrains as additional field variables through global energy-minimization frameworks that rely on the symbolic differentiation and optimization capabilities of the programming libraries used. This introduces additional global degrees of freedom, requires specialized software, and makes integration into standard finite-element codes, where constitutive models are evaluated pointwise at integration points, non-trivial. As a result, these formulations have so far only been demonstrated on simple academic configurations.

The present work builds directly on these eigenstrain-based formulations, and does not claim the fracture eigenstrains, explicit strength surfaces, or the decoupling of crack nucleation from fracture energy as new model ingredients. The contribution is instead computational: the eigenstrain evolution is reformulated as a local constitutive update at each integration point, rather than as additional global field variables. This local return-mapping strategy is analogous to standard plasticity algorithms, making the formulation compatible with conventional finite-element implementations and allowing consistent tangent operators to be derived for smooth and non-smooth strength surfaces. The resulting formulation is applied to standard phase-field benchmark problems, including mesh-refinement studies, mixed-mode crack propagation, and dynamic crack branching, rather than being restricted to the mathematical and small-scale test cases considered so far. To the author's knowledge, this is the first such demonstration for this class of cohesive phase-field models.

To realise this local formulation, the work focuses on: (i) defining eigenstrain directions for each strength criterion, including a new Drucker-Prager-like criterion that captures pressure-dependent strengthening under compression, (ii) deriving consistent tangent operators in closed form for both smooth and non-smooth strength surfaces, handling the non-trivial switching between active and inactive failure modes, and (iii) addressing the numerical conditioning challenges that arise from the near-singular tangent matrices at the onset of fracture. The energy expressions and governing equations are described in Section 2, followed by a detailed description of the return-mapping scheme and its consistent tangent stiffness matrix in Section 3. The benchmark problems used to assess these properties are then presented in Section 4. All codes used for these benchmark cases are openly available, allowing for building upon or using the models for other applications, see the data availability section at the end of this paper. Throughout this work, italic symbols denote scalars, bold-upright symbols denote vectors, and bold-italic symbols denote matrices. Stress tensors are denoted in bold-italic, while their Mandel-vector representations are denoted in bold-upright.

2. Governing equations

We consider a domain Ω, described through the displacement $\mathbf{u}$ and the phase-field parameter ϕ. ϕ indicates the loss of cohesive strength with $\phi = 0$ indicating a fully intact material and $\phi = 1$ indicating a full loss of strength. This is in contrast to standard phase-field descriptions where it is used to indicate the presence of cracks through a loss of the stiffness. Following the method from [35], the elastic strains are composed of a displacement component and a fracture-eigenstrain component, using a small-strains assumption:

$$\boldsymbol{\varepsilon}_{\mathrm{el}} = \boldsymbol{\varepsilon} - \boldsymbol{\eta} = \nabla^s \mathbf{u} - \boldsymbol{\eta} \tag{1}$$

where the eigenstrains $\boldsymbol{\eta}$ allow for the representation of crack-like behaviour, by reducing the elastic strains to represent the reduced stresses transferred through crack surfaces. This $\boldsymbol{\eta}$ is zero when no cracks are present, is a small factor of $\boldsymbol{\varepsilon}$ at the onset of cracks where the crack still allows for the transfer of stress through the cohesive zone, and evolves to a comparable magnitude as the total strains once the crack opening exceeds the cohesive length. This eigenstrain is also used to enforce different behaviour normal and tangential to the crack surface, e.g. allowing for normal stresses to represent self-contact under compression while removing the transfer of shear stresses.

Throughout this work, we assume a linear-elastic bulk behaviour, such that the elastic energy stored in the material is given as a function of the elastic strains, Eq. (1), as:

$$\Psi_{\mathrm{el}} = \int_\Omega \frac{1}{2} K \mathrm{tr}^2(\boldsymbol{\varepsilon} - \boldsymbol{\eta}) + \mu \|\mathrm{dev}(\boldsymbol{\varepsilon} - \boldsymbol{\eta})\|^2 \, \mathrm{d}\Omega \tag{2}$$

using the bulk modulus K and the shear modulus μ. tr indicates the trace operator, while dev() is used to indicate that only the deviatoric component of the strains is used, $\mathrm{dev}(\boldsymbol{\varepsilon}) = \boldsymbol{\varepsilon} - \frac{1}{3}\mathrm{tr}(\boldsymbol{\varepsilon})\boldsymbol{I}$. $\|\varepsilon\|$ indicates the L_2 norm, $\|\boldsymbol{\varepsilon}\|^2 = \boldsymbol{\varepsilon} : \boldsymbol{\varepsilon}$. We note that the use of a linear-elastic, small-strain model is not a fundamental requirement of the presented framework, and more general constitutive models could in principle be incorporated in a similar manner as in standard phase-field models (e.g. finite strain [37–39] or hyperelasticity models [40–43]). The assumption of linear elasticity is made here for simplicity and to focus on the implementation of the cohesive phase-field fracture model. The same solution scheme could in principle be combined with more complex bulk constitutive

models or material descriptions, but doing so would require problem-specific choices that are separate from the implementation issue addressed here. For example, for finite-strain or nonlinear material models, the fracture eigenstrains, stress measures, and tangent operators would need to be reformulated consistently within the chosen kinematic setting before being incorporated into the same local-update structure, while heterogeneous or interfacial fracture would require additional assumptions on how the strength surface and fracture energy vary across material interfaces. These questions are therefore not pursued in the present manuscript, which uses homogeneous small-strain benchmark problems to isolate and verify the proposed return-mapping based formulation.

The fracture energy release rate, G_c, indicates the rate at which energy is released during fracture propagation, with low values of G_c corresponding to brittle behaviour while higher values typically lead to a more ductile/cohesive type of fracture. Using this fracture energy, the energy dissipated through the opening of fractures is defined as [44, 45]:

$$\Psi_\mathrm{c} = \int_{\Gamma_\mathrm{c}} G_\mathrm{c}\, \mathrm{d}\Gamma_\mathrm{c} \approx \int_\Omega \gamma(\phi) G_\mathrm{c}\, \mathrm{d}\Omega \qquad \frac{\partial \gamma(\phi) G_\mathrm{c}}{\partial t} \geq 0 \tag{3}$$

with the KKT irreversibility condition ensuring that this is a purely dissipative mechanism [46]. The phase-field distribution function $\gamma(\phi)$ is used to distribute the energy released by a discrete crack over a finite region surrounding the crack. Specifically, a quadratic, AT2-type [47], phase-field distribution function is used, given by:

$$\gamma(\phi) = \frac{1}{2\ell}\left(\phi^2 + \ell^2 |\nabla\phi|^2\right) \tag{4}$$

using the length scale ℓ. This length scale indicates the region over which the loss of cohesive strength is distributed. Through the introduction of this length scale, mesh-size independent results can be attained even though the eigenstrains representing the crack are localized. We note that the choice to use an AT-2 model was made to not impose an additional strength criterion on top of the strength potentials defined in Section 2.2. Instead, using an AT-1 model would require the eigenstrains to exceed a certain length-scale dependent threshold before the phase-field variable can increase, thus resulting in initial cracks not starting to lose cohesion until this threshold is reached. As the eigenstrains are used to represent the crack opening, this would result in a non-physical behaviour where cracks can open without losing cohesion until a certain crack opening is reached. An AT-2 model does not have this issue, as the phase-field variable can increase as soon as the eigenstrains start to develop, allowing for a more physical representation of the cohesive behaviour.

To link the phase-field functions and the fracture eigenstrains, a material strength potential is introduced [35]. As will be shown later, the derivative of this potential will define the maximum stress that can be sustained by the material, and how this degrades as the phase-field parameter increases. The energy contribution of this strength potential is given by:

$$\Psi_\mathrm{f} = \int_\Omega F(\boldsymbol{\eta})\, \mathrm{d}\Omega = \int_\Omega d(\phi) F_\mathrm{d}(\boldsymbol{\eta}) + F_\mathrm{i}(\boldsymbol{\eta})\, \mathrm{d}\Omega \tag{5}$$

with the potentials F_d and F_i used in Section 2.2 to define the strength of the material and the non-penetration condition respectively. The degradation function is defined in a standard manner:

$$d(\phi) = (1-\kappa)(1-\phi)^2 + \kappa \tag{6}$$

such that the full strength potential F_d is used to describe the intact material, while degrading this potential based on the phase-field parameter to represent the loss of cohesion as the cohesive crack evolves. The parameter κ is used

to provide a residual strength, preventing the strength potentials from degrading fully such that their derivatives remain well-defined. We note that this differs from standard phase-field formulations, where κ is a residual stiffness.

Finally, we include dynamic effects through inertia and damping energy contributions, and loading through the body and external forces energy contributions:

$$\Psi_{\mathrm{i}} = \int_{\Omega} \frac{1}{2}\rho\dot{\mathbf{u}}^2 \,\mathrm{d}\Omega + \int_t \int_{\Omega} \frac{1}{2}\rho c\dot{\mathbf{u}}^2 \,\mathrm{d}t\mathrm{d}\Omega \qquad \Psi_{\mathrm{b}} = \int_{\Omega} \mathbf{b}^{\top}\mathbf{u} \,\mathrm{d}\Omega + \int_{\Gamma} \boldsymbol{\tau}^{\top}\mathbf{u} \,\mathrm{d}\Gamma \tag{7}$$

using the density ρ, body forces $\mathbf{b}$, and external traction $\boldsymbol{\tau}$. Within the subsequent examples, the damping is included to limit the impact of stress waves due to sudden material failure when considering cases under slow loading, whereas for cases explicitly considering dynamic loading it is set to zero. The inclusion of inertia, even for slow loading, helps with spreading the crack propagation over multiple time increments, preventing the need to resolve cracks propagating through the full domain within a single time/load step. Body forces are included within this derivation for completeness, but are set to $\mathbf{b} = \mathbf{0}$ in the benchmark cases considered.

2.1. Energy minimization

The governing equations follow from minimizing the energies contained within the material, Eqs. (2), (3), (5) and (7):

$$\min\left(\Psi(\mathbf{u}, \boldsymbol{\eta}, \phi)\right) = \min(\Psi_{\mathrm{el}} + \Psi_{\mathrm{c}} + \Psi_{\mathrm{f}} - \Psi_{\mathrm{i}} - \Psi_{\mathrm{b}}) \tag{8}$$

This is the total energy expression proposed by Vicentini et al. [35], who minimize it directly using a global optimization framework that treats $\mathbf{u}$, $\boldsymbol{\eta}$, and ϕ as independent field variables. In the present work, we instead derive the governing equations and constitutive relations that follow from this energy, and resolve the eigenstrain evolution locally at each integration point. The governing equations are given through the derivatives with regards to the displacement $\mathbf{u}$ and phase-field parameter ϕ. First, using the derivative with respect to $\mathbf{u}$, we obtain the weak form of the momentum balance:

$$0 = \frac{\partial \Psi}{\partial \mathbf{u}} = \int_{\Omega} \delta\mathbf{u}^{\top} \left(-\nabla \cdot \boldsymbol{\sigma} + \rho c\dot{\mathbf{u}} + \rho\ddot{\mathbf{u}} - \mathbf{b}\right) \,\mathrm{d}\Omega \tag{9}$$

where integration by parts has been used to obtain the divergence of stress term, to more clearly convey the strong form relations. When producing the finite element forms in Section 3, this will be reversed to remove the need to obtain stress gradients. Next, using the derivative of the total energy with respect to ϕ, we obtain the weak form of the phase-field evolution:

$$0 = \frac{\partial \Psi}{\partial \phi} = \int_{\Omega} \delta\phi \left(\frac{G_{\mathrm{c}}}{\ell}(\phi - \ell^2\nabla^2\phi) + \frac{\partial d(\phi)}{\partial \phi}\mathcal{F} \right) \,\mathrm{d}\Omega \tag{10}$$

Within this relation, the irreversibility condition is enforced by using the history parameter $\mathcal{F}$, defined as the maximum achieved crack driving force:

$$\mathcal{F}^{t+\Delta t}(\boldsymbol{\eta}) = \max(F_{\mathrm{d}}^{t+\Delta t}(\boldsymbol{\eta}), \mathcal{F}^{t}) \tag{11}$$

where the superscripts $t + \Delta t$ and t are used to indicate the current and previous discrete time steps respectively. This history parameter ensures the crack formation is a purely dissipative mechanism, ensuring that the phase-field parameter ϕ can only increase, and thus the strength potential can only degrade, as the crack evolves.

In addition to these governing equations, the constitutive models result from minimizing the total energy with regard to our internal variables, the total strains and fracture eigenstrains. Considering the total strains results in the constitutive models for the elastic stresses:

$$\boldsymbol{\sigma} = \frac{\partial \Psi}{\partial \boldsymbol{\varepsilon}} = K\mathrm{tr}(\boldsymbol{\varepsilon} - \boldsymbol{\eta})\boldsymbol{I} + 2\mu\mathrm{dev}(\boldsymbol{\varepsilon} - \boldsymbol{\eta}) \tag{12}$$

and considering the fracture-eigenstrain results in the material strength criterion:

$$\mathbf{0} \leq \frac{\partial \Psi}{\partial \boldsymbol{\eta}} = -\left(K\mathrm{tr}(\boldsymbol{\varepsilon} - \boldsymbol{\eta})\boldsymbol{I} + 2\mu\mathrm{dev}(\boldsymbol{\varepsilon} - \boldsymbol{\eta})\right) + d(\phi)\frac{\partial F_\mathrm{d}(\boldsymbol{\eta})}{\partial \boldsymbol{\eta}} + \frac{\partial F_\mathrm{i}(\boldsymbol{\eta})}{\partial \boldsymbol{\eta}} = d(\phi)\frac{\partial F_\mathrm{d}(\boldsymbol{\eta})}{\partial \boldsymbol{\eta}} + \frac{\partial F_\mathrm{i}(\boldsymbol{\eta})}{\partial \boldsymbol{\eta}} - \boldsymbol{\sigma} \tag{13}$$

This constitutive model requires that the stress state of intact material remains within or on the derivative of the strength potential functions, $d(\phi)\frac{\partial F_\mathrm{d}(\boldsymbol{\eta})}{\partial \boldsymbol{\eta}} + \frac{\partial F_\mathrm{i}(\boldsymbol{\eta})}{\partial \boldsymbol{\eta}} \geq \boldsymbol{\sigma}$. When the stress reaches this potential surface, the eigenstrains develop to retain the stress on the potential surface, while increasing the phase-field driving force $\mathcal{F}$. This then allows the phase-field variable ϕ to increase, decreasing the damage function d such that the strength potential reduces. As such, the strength criterion decreases, representing the loss of cohesion as the eigenstrain (and thus the crack opening) increases.

For the direction of the eigenstrains, we define these to follow the directions of the strains $\boldsymbol{\varepsilon}$ through a function $\boldsymbol{G}$, such that:

$$\boldsymbol{\eta} = \lambda \boldsymbol{G}(\boldsymbol{\varepsilon}) \tag{14}$$

in the case of a smooth failure surface, or in the case of a surface composed of multiple facets, using:

$$\boldsymbol{\eta} = \sum_i \lambda_i \boldsymbol{G}_i(\boldsymbol{\varepsilon}) \tag{15}$$

using the multipliers λ to indicate the magnitude of the eigenstrains. Using these directions based on the strains $\boldsymbol{\varepsilon}$ allows the eigenstrains $\boldsymbol{\eta}$ to follow the same direction, thereby ensuring that the eigenstrains always act to reduce the total strains. As a result, we can reduce the strength criterion from Eq. (13) to solely require the stresses in the direction of the currently applied strains not to exceed the fracture surface. This results in:

$$0 \leq \frac{\partial \Psi}{\partial \lambda_i} = \frac{\partial \boldsymbol{\eta}}{\partial \lambda_i} : \frac{\partial \Psi}{\partial \boldsymbol{\eta}} = \left(\frac{\partial \boldsymbol{\eta}}{\partial \lambda_i}\right) : \left(d(\phi)\frac{\partial F_\mathrm{d}(\boldsymbol{\eta})}{\partial \boldsymbol{\eta}} + \frac{\partial F_\mathrm{i}(\boldsymbol{\eta})}{\partial \boldsymbol{\eta}} - \boldsymbol{\sigma}\right) \tag{16}$$

This criterion only requires the stresses to be within the failure surface in the potential directions of unloading, thereby solely requiring the multipliers λ to be resolved rather than all components of $\boldsymbol{\eta}$. It should also be noted that, as no spatial gradients of the eigenstrains are required, these multipliers can be solved on a point-by-point basis, rather than requiring λ to be resolved as a complete field. As a result, the constitutive models can be resolved in a similar manner as for plasticity schemes, using an integration-point-local return mapping scheme.

2.2. Strength potentials

Here, we will consider two combinations of strength potential and eigenstrain directions. The first is the $r1$ criterion used by Vicentini et al. [35], defined through the tensile strength f_t and the shear strength f_s:

$$F_\mathrm{d} = f_\mathrm{t}\left\langle \mathrm{tr}(\boldsymbol{\eta})\right\rangle^+ + f_\mathrm{s}\|\mathrm{dev}(\boldsymbol{\eta})\| \qquad F_\mathrm{i} = -10^6 f_\mathrm{t}\left\langle \mathrm{tr}(\boldsymbol{\eta})\right\rangle^- \tag{17a}$$

$$\boldsymbol{G}_1 = \frac{1}{3}\frac{\mathrm{tr}(\boldsymbol{\varepsilon})}{|\mathrm{tr}(\boldsymbol{\varepsilon})|}\boldsymbol{I} \qquad \boldsymbol{G}_2 = \frac{\mathrm{dev}(\boldsymbol{\varepsilon})}{\|\mathrm{dev}(\boldsymbol{\varepsilon})\|} \tag{17b}$$

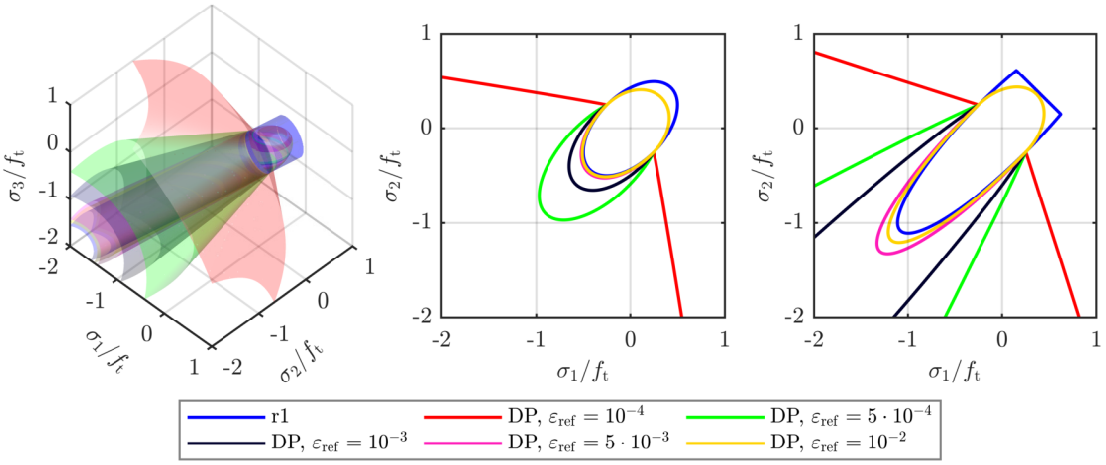

(a) Principal stress space (b) Plane-stress ($\sigma_3 = 0$) (c) Plane-strain ($\varepsilon_3 = 0$)

Figure 1: Strength surfaces for a fully intact material ($\phi = 0$) using $f_s = 0.5 f_t$, with the $r1$ criterion, Eq. (17), shown in blue, and the other colours indicating the Drucker-Prager-like criteria, Eq. (18), using different values for ε_{ref}.

where the Macaulay brackets $\langle \square \rangle^+$ and $\langle \square \rangle^-$ are used to indicate that this term is only non-zero if the quantity is positive/negative respectively, thereby enforcing a different behaviour under compression/tension. Specifically, the compressive strength is set to $-10^6\times$ the tensile strength, and this compressive strength is not degraded, thereby ensuring that even when the material is fully damaged, $d \approx 0$, it still correctly enforces a non-penetration condition on contact. Furthermore, this compressive strength is set to be negative, such that once projected in the compressive direction, it produces a positive value. The directions for the eigenstrains, $\boldsymbol{G}_1$ and $\boldsymbol{G}_2$, are used in a normalized form, such that λ_i directly dictates the magnitude of these strains. This failure criterion is shown in Fig. 1 as a blue line, with the compressive strength limit/non-penetration condition, resulting from F_i, not shown as this falls far outside the limits of the plot.

The second strength potential used is a combination of the $r2$ criterion from [35] under tension, and a Drucker-Prager-like cone under compression. This function is defined through the tensile and shear strengths and an additional parameter ε_{ref} that dictates the strength increase under compression:

$$F_d = \begin{cases} \sqrt{f_t^2 \mathrm{tr}^2(\boldsymbol{\eta}) + f_s^2 \|\mathrm{dev}(\boldsymbol{\eta})\|^2} & \text{if} \quad \mathrm{tr}(\boldsymbol{\varepsilon}) \geq 0 \\ f_s \left(1 - \frac{\mathrm{tr}(\boldsymbol{\varepsilon})}{\varepsilon_{ref}}\right) \|\mathrm{dev}(\boldsymbol{\eta})\| & \text{if} \quad \mathrm{tr}(\boldsymbol{\varepsilon}) < 0 \end{cases} \tag{18a}$$

$$\boldsymbol{G} = \begin{cases} \frac{\boldsymbol{\varepsilon}}{\|\boldsymbol{\varepsilon}\|} & \text{if} \quad \mathrm{tr}(\boldsymbol{\varepsilon}) \geq 0 \\ \frac{\mathrm{dev}(\boldsymbol{\varepsilon})}{\|\mathrm{dev}(\boldsymbol{\varepsilon})\|} & \text{if} \quad \mathrm{tr}(\boldsymbol{\varepsilon}) < 0 \end{cases} \tag{18b}$$

As we explicitly enforce that the eigenstrains are in the deviatoric direction under compression through $\boldsymbol{G}$, we do not need to separately enforce non-penetration conditions. Altering the direction of the admissible fracture eigenstrains under compression achieves the same as the penalty term within Eq. (17): Allowing for shear cracks while preventing volume changes and thus the crack faces from interpenetrating. We also note the presence of the strains $\boldsymbol{\varepsilon}$ within the definition of the strength potential, which is required to obtain the strengthening effect under

compression. As $\mathrm{tr}(\boldsymbol{\eta}) \geq 0$ per definition, $\boldsymbol{\eta}$ cannot be used to define the compressive strains acting on the material. This failure surface is shown in Fig. 1 for different values of $\varepsilon_{\mathrm{ref}}$.

3. Computational implementation

The governing equations, Eqs. (9) and (10), are solved using the finite element method, discretizing the displacement and phase-field variable as:

$$\mathbf{u} = \sum_{\mathrm{el}} \boldsymbol{N}_{\mathrm{u}} \mathbf{u}_{\mathrm{n}} \qquad \phi = \sum_{\mathrm{el}} \mathbf{N}_{\phi} \boldsymbol{\phi}_{\mathrm{n}} \tag{19}$$

using quadratic Lagrange elements for both the displacements, $\boldsymbol{N}_{\mathrm{u}}$, and the phase-field, $\mathbf{N}_{\phi}$. $\mathbf{u}_{\mathrm{n}}$ and the phase-field $\boldsymbol{\phi}_{\mathrm{n}}$ are the nodal values for the displacement and phase-field for the specific element being considered. For notational convenience of the derivatives of the strength surface, and the resulting tangent stiffness matrix, we will use Mandel notation, defining the relation between displacements and strains as:

$$\boldsymbol{\varepsilon} = \begin{bmatrix} \varepsilon_{xx} & \varepsilon_{yy} & \varepsilon_{zz} & \sqrt{2}\varepsilon_{yz} & \sqrt{2}\varepsilon_{xz} & \sqrt{2}\varepsilon_{xy} \end{bmatrix}^{\top} = \boldsymbol{L}\boldsymbol{N}_{\mathrm{u}}\mathbf{u}_{\mathrm{n}} \tag{20}$$

where $\boldsymbol{L}$ is the displacement-to-strain mapping matrix. Using this discretization, the weak forms of the governing equation are discretized as:

$$\mathbf{F}_{\mathrm{u}} = \int_{\Omega} \boldsymbol{N}_{\mathrm{u}}^{\top} \boldsymbol{L}^{\top} \boldsymbol{\sigma} + \rho c \boldsymbol{N}_{\mathrm{u}}^{\top} \boldsymbol{N}_{\mathrm{u}} \dot{\mathbf{u}}_{\mathrm{n}} + \rho \boldsymbol{N}_{\mathrm{u}}^{\top} \boldsymbol{N}_{\mathrm{u}} \ddot{\mathbf{u}}_{\mathrm{n}} + \boldsymbol{N}_{\mathrm{u}}^{\top} \mathbf{b} \, \mathrm{d}\Omega + \int_{\Gamma} \boldsymbol{N}_{\mathrm{u}}^{\top} \boldsymbol{\tau} \, \mathrm{d}\Gamma = \mathbf{0} \tag{21}$$

$$\mathbf{F}_{\phi} = \int_{\Omega} \frac{G_{\mathrm{c}}}{\ell} \mathbf{N}_{\phi}^{\top} \mathbf{N}_{\phi} \boldsymbol{\phi}_{\mathrm{n}} + G_{\mathrm{c}} \ell \left(\nabla \mathbf{N}_{\phi}\right)^{\top} \nabla \mathbf{N}_{\phi} \boldsymbol{\phi}_{\mathrm{n}} - 2(1-\kappa) \mathbf{N}_{\phi}^{\top} (1 - \mathbf{N}_{\phi}^{\top} \boldsymbol{\phi}_{\mathrm{n}}) \mathcal{F} \, \mathrm{d}\Omega = \mathbf{0} \tag{22}$$

where the stresses $\boldsymbol{\sigma}$ (and the tangent stiffness matrix required for the non-linear solver) and the crack driving force $\mathcal{F}$ are calculated within each integration point through a return-mapping scheme, similarly as is standard within plasticity models. A multi-pass staggered solution scheme is used, solving for the displacements and fracture eigenstrains first, then solving for the phase-field, and iterating several times until both fields are converged (or a maximum of 5 passes have been performed). A Newmark scheme is used for the time discretization of the displacements, using time-integration parameters $\beta = 0.5625$ and $\gamma = 1.0$. These values for the time-integration are chosen to enforce sufficient numerical damping, preventing stress waves travelling through the complete domain and reflecting on the boundaries. The discretized equations are implemented using the finite-element programming library FEniCSx [48], together with the numba library [49] for the calculation of per-integration-point quantities, and the codes used to generate all results are openly available (see data availability at the end of this paper). The resulting staggered global solve and local integration-point update are summarized in Algorithm 1.

3.1. Return mapping scheme

The strength criterion, Eq. (16), together with the relation between stresses and elastic energy, Eq. (12), are solved within each integration point. First considering the case with a single eigenstrain direction, e.g. Eq. (18), this scheme is described through the two residuals:

$$f_1 = 0 = \boldsymbol{\sigma} - \frac{\partial \Psi_{\mathrm{el}}}{\partial \boldsymbol{\varepsilon}} = 0 \tag{23a}$$

$$f_2 = 0 = \begin{cases} \lambda & \text{if} \quad \left(\frac{\partial \boldsymbol{\eta}}{\partial \lambda}\right)^{\top} \left(\frac{\partial F}{\partial \boldsymbol{\eta}} - \boldsymbol{\sigma}\right) > 0 \\ \left(\frac{\partial \boldsymbol{\eta}}{\partial \lambda}\right)^{\top} \left(\frac{\partial F}{\partial \boldsymbol{\eta}} - \boldsymbol{\sigma}\right) + \kappa_{\mathrm{t}} K \lambda & \text{otherwise} \end{cases} \tag{23b}$$

Algorithm 1 Staggered finite-element solution with local return mapping

for each time/load step $t + \Delta t$ **do**
  Initialize $\mathbf{u}^{t+\Delta t}$, $\phi^{t+\Delta t}$, and $\mathcal{F}^{t+\Delta t}$ from the converged state at t
  for staggered pass $k = 1, \ldots, k_{\max}$ **do**
    Start the Newton-Raphson solve of the displacement problem
    for each Newton iteration of the displacement solve **do**
      for each integration point **do**
        Compute the strain $\boldsymbol{\varepsilon}$ from the current displacement $\mathbf{u}^{t+\Delta t}$
        Determine the active strength-surface condition
        Solve the local return-mapping problem for λ or λ_i
        Return $\boldsymbol{\sigma}$ and $\boldsymbol{D}_{\tan}$ to the displacement residual and Jacobian, and store $\mathcal{F}$
      end for
      Assemble and solve the linearized global Newton system
      Update the displacement iterate $\mathbf{u}^{t+\Delta t}$
      if the displacement residual has converged **then**
        Break
      end if
    end for
    Solve the phase-field problem using the updated history field $\mathcal{F}$
    if the staggered fields have converged **then**
      Break
    end if
  end for
end for

where the $f_2 = \lambda$ condition is used when the stresses are within the failure criterion, enforcing $\lambda = 0$, while the second criterion solves for λ such that the stresses are on the fracture criterion. A small additional factor $\kappa_t K \lambda$ is added to the second equation, with this term providing a residual stiffness post-fracture by extending the failure surface based on the magnitude of the fracture eigenstrains. This stiffness is needed in addition to the residual strength κ from Eq. (6) to ensure no unconstrained degrees of freedom arise when the stresses are on the strength surface.

The system of equations from Eq. (23) is solved using an iterative Newton-Raphson scheme, described in the case where the stresses exceed the failure function by:

$$\boldsymbol{K} \begin{bmatrix} \mathrm{d}\boldsymbol{\sigma} \\ \mathrm{d}\lambda \end{bmatrix} = - \begin{bmatrix} f_1 \\ f_2 \end{bmatrix} \qquad \text{where} \qquad \boldsymbol{K} = \begin{bmatrix} \boldsymbol{I} & \frac{\partial^2 \Psi}{\partial \boldsymbol{\varepsilon}^2} \frac{\partial \boldsymbol{\eta}}{\partial \lambda} \\ \left(\frac{\partial \boldsymbol{\eta}}{\partial \lambda} \right)^\top & \kappa_t K \end{bmatrix} \tag{24}$$

using the tangent matrix $\boldsymbol{K}$. This matrix is also used in constructing a consistent tangent stiffness matrix as:

$$\begin{bmatrix} \frac{\partial \boldsymbol{\sigma}}{\partial \boldsymbol{\varepsilon}} \\ \frac{\partial \lambda}{\partial \varepsilon} \end{bmatrix} = \boldsymbol{K}^{-1} \begin{bmatrix} -\frac{\partial^2 \Psi}{\partial \boldsymbol{\varepsilon}^2} \\ 0 \end{bmatrix} \tag{25}$$

where the top (6×6) sub-matrix, corresponding to the $\frac{\partial \boldsymbol{\sigma}}{\partial \boldsymbol{\varepsilon}}$, is used within the non-linear solving scheme for the momentum balance, Eq. (21). For this case, where only a single direction of the fracture eigenstrains is used, this tangent stiffness matrix can also be explicitly expressed in terms of the direction of the eigenstrains as:

$$\boldsymbol{D}_{\text{tan}} = \frac{\partial^2 \Psi_{\text{el}}}{\partial \boldsymbol{\varepsilon}^2} \left(\boldsymbol{I} - \frac{\frac{\partial^2 \Psi_{\text{el}}}{\partial \boldsymbol{\varepsilon}^2} \frac{\partial \boldsymbol{\eta}}{\partial \lambda} \left(\frac{\partial \boldsymbol{\eta}}{\partial \lambda} \right)^\top}{\left(\frac{\partial \boldsymbol{\eta}}{\partial \lambda} \right) \frac{\partial^2 \Psi_{\text{el}}}{\partial \boldsymbol{\varepsilon}^2} \frac{\partial \boldsymbol{\eta}}{\partial \lambda} + \kappa_{\text{t}} K} \right) \tag{26}$$

which clearly shows the role of the residual stiffness κ_{t}. Without this term, as soon as the stresses exceed the strength surface the stiffness in the direction of the eigenstrains becomes zero. By including this term, the stiffness is set to a small value, avoiding issues with ill-constrained degrees of freedom. Furthermore, this slight offset from the strength surface also helps the iterative scheme from Eq. (23) by preventing the state from alternating between two conditions due to trying to return to the surface exactly.

If instead we consider a non-smooth fracture criterion, e.g. Eq. (17), where the strength criterion is checked and the eigenstrain develops in multiple independent directions, the residuals are defined in terms of stresses $\boldsymbol{\sigma}$, and the two eigenstrain magnitudes λ_1 and λ_2 as:

$$f_1 = 0 = \boldsymbol{\sigma} - \frac{\partial \Psi_{\text{el}}}{\partial \boldsymbol{\varepsilon}} = 0 \tag{27a}$$

$$f_2 = 0 = \begin{cases} \lambda_1 & \text{if} \quad \left(\frac{\partial \boldsymbol{\eta}}{\partial \lambda_1} \right)^\top \left(\frac{\partial F}{\partial \boldsymbol{\eta}} - \boldsymbol{\sigma} \right) > 0 \\ \left(\frac{\partial \boldsymbol{\eta}}{\partial \lambda_1} \right)^\top \left(\frac{\partial F}{\partial \boldsymbol{\eta}} - \boldsymbol{\sigma} \right) + \kappa_{\text{t}} K \lambda_1 & \text{otherwise} \end{cases} \tag{27b}$$

$$f_3 = 0 = \begin{cases} \lambda_2 & \text{if} \quad \left(\frac{\partial \boldsymbol{\eta}}{\partial \lambda_2} \right)^\top \left(\frac{\partial F}{\partial \boldsymbol{\eta}} - \boldsymbol{\sigma} \right) > 0 \\ \left(\frac{\partial \boldsymbol{\eta}}{\partial \lambda_2} \right)^\top \left(\frac{\partial F}{\partial \boldsymbol{\eta}} - \boldsymbol{\sigma} \right) + \kappa_{\text{t}} K \lambda_2 & \text{otherwise} \end{cases} \tag{27c}$$

where for each direction the stresses need to stay within the individual strength surfaces, in this case separately checking for the volumetric and shear components. Following from these residuals, assuming eigenstrains develop in both directions the iterative solution scheme is given as:

$$\boldsymbol{K} \begin{bmatrix} \mathrm{d}\boldsymbol{\sigma} \\ \mathrm{d}\lambda_1 \\ \mathrm{d}\lambda_2 \end{bmatrix} = - \begin{bmatrix} f_1 \\ f_2 \\ f_3 \end{bmatrix} \quad \text{where} \quad \boldsymbol{K} = \begin{bmatrix} \boldsymbol{I} & \frac{\partial^2 \Psi}{\partial \boldsymbol{\varepsilon}^2} \frac{\partial \boldsymbol{\eta}}{\partial \lambda_1} & \frac{\partial^2 \Psi}{\partial \boldsymbol{\varepsilon}^2} \frac{\partial \boldsymbol{\eta}}{\partial \lambda_2} \\ \left(\frac{\partial \boldsymbol{\eta}}{\partial \lambda_1} \right)^\top & \kappa_{\text{t}} K & 0 \\ \left(\frac{\partial \boldsymbol{\eta}}{\partial \lambda_2} \right)^\top & 0 & \kappa_{\text{t}} K \end{bmatrix} \tag{28}$$

If instead, only one of the failure criteria is exceeded, the tangent matrix becomes:

$$\boldsymbol{K} = \begin{bmatrix} \boldsymbol{I} & \frac{\partial^2 \Psi}{\partial \boldsymbol{\varepsilon}^2} \frac{\partial \boldsymbol{\eta}}{\partial \lambda_1} & \frac{\partial^2 \Psi}{\partial \boldsymbol{\varepsilon}^2} \frac{\partial \boldsymbol{\eta}}{\partial \lambda_2} \\ \left(\frac{\partial \boldsymbol{\eta}}{\partial \lambda_1} \right)^\top & \kappa_{\text{t}} K & 0 \\ 0 & 0 & 1 \end{bmatrix} \quad \text{or} \quad \boldsymbol{K} = \begin{bmatrix} \boldsymbol{I} & \frac{\partial^2 \Psi}{\partial \boldsymbol{\varepsilon}^2} \frac{\partial \boldsymbol{\eta}}{\partial \lambda_1} & \frac{\partial^2 \Psi}{\partial \boldsymbol{\varepsilon}^2} \frac{\partial \boldsymbol{\eta}}{\partial \lambda_2} \\ 0 & 1 & 0 \\ \left(\frac{\partial \boldsymbol{\eta}}{\partial \lambda_2} \right)^\top & 0 & \kappa_{\text{t}} K \end{bmatrix} \tag{29}$$

when eigenstrains only develop in the λ_1 or λ_2 directions respectively. An explicit expression for the tangent stiffness matrix follows from using the Schur complement:

$$\boldsymbol{D}_{\text{tan}} = \frac{\partial^2 \Psi_{\text{el}}}{\partial \boldsymbol{\varepsilon}^2} \left(\boldsymbol{I} - \frac{\partial^2 \Psi_{\text{el}}}{\partial \boldsymbol{\varepsilon}^2} \boldsymbol{g} \boldsymbol{S}^{-1} \mathbf{g}^\top \right) \quad \text{where} \quad \mathbf{g} = \begin{bmatrix} \frac{\partial \boldsymbol{\eta}}{\partial \lambda_1} & \frac{\partial \boldsymbol{\eta}}{\partial \lambda_2} \end{bmatrix} \quad \text{and} \quad \boldsymbol{S} = \mathbf{g}^\top \frac{\partial^2 \Psi_{\text{el}}}{\partial \boldsymbol{\varepsilon}^2} \mathbf{g} - \begin{bmatrix} \kappa_{\text{t}} K & 0 \\ 0 & \kappa_{\text{t}} K \end{bmatrix} \tag{30}$$

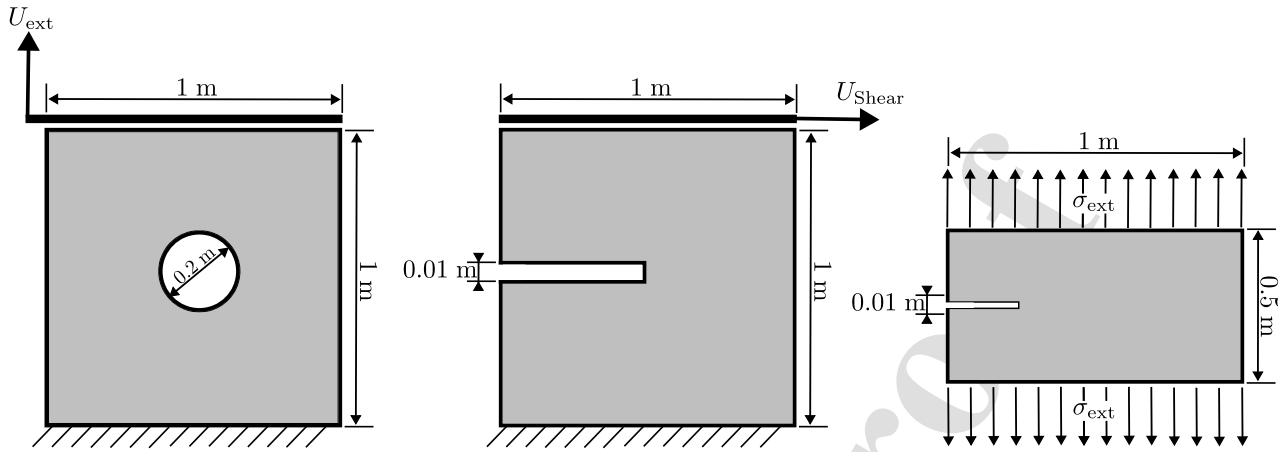

(a) Plate with hole (b) Single edge notched plate (c) Dynamic fractures

Figure 2: Geometries and boundary conditions considered for the example cases.

If only the strength in one of the eigenstrain directions is exceeded, the direction that corresponds to the intact strength in $\mathbf{g}$ is set to zero and the diagonal term is set to one to obtain the tangent stiffness. We note that the use of a Schur complement, rather than directly calculating the inverse of the $\boldsymbol{K}$ matrix is needed due to the poor conditioning of this matrix. Convergence issues were encountered using $\boldsymbol{K}^{-1}$, whereas no such issues were seen using the Schur complement which obtained well-converging results for all cases considered, with convergence rates between linear at the onset of fractures and quadratic when no new integration points start to fracture. Detailed residual histories are not reported here because they depend on the time/load increment (larger increments require more iterations), mesh, and active crack-growth state (crack nucleation and bifurcation), and therefore do not provide a problem-independent convergence benchmark. However, the solver settings and scripts used for all examples are included in the openly available source code, allowing the nonlinear convergence histories to be generated and inspected for each benchmark case.

4. Benchmark cases

To demonstrate the capabilities of the presented model, and explore the required element sizes, and influence of model parameters, we will consider the three cases shown in Fig. 2: A plate with a hole under tension, a notched specimen under shear, and a notched specimen under dynamic loading. All cases use the same material parameters, shown in Table 1, unless stated otherwise, and all cases assume plane-strain conditions.

4.1. Plate with hole

The first case considered consists of a unit square with a hole with a diameter of 0.2 m in the centre. The bottom of the domain is fixed in horizontal and vertical direction, while a displacement is imposed at the top surface at a rate of $\dot{U}_{\text{ext}} = \pm 3 \cdot 10^{-6}$ m/s. This strain rate is chosen low to limit the impact of inertia for most cases, with it only affecting the obtained results for cases showing a snap-back type behaviour where the material suddenly fails. Loading under either tension (upwards displacement) or compression (downwards displacement) are considered. Due to the stress concentrations at the side of the hole, and the equal tensile and shear strength, cracks should form

Young's modulus	E	200	GPa
Poisson ratio	ν	0.3	
Tensile strength	f_{t}	150	MPa
Shear strength	f_{s}	150	MPa
Fracture release energy	G_{c}	100	kJ/m^2
Phase-field length scale	ℓ	0.05	m
Density	ρ	8000	kg/m^3
Damping coefficient	c	10^6	s^{-1}
Residual strength	κ	10^{-3}	
Residual stiffness	κ_{t}	10^{-9}	

Table 1: Material properties used unless otherwise stated for Sections 4.1-4.3.

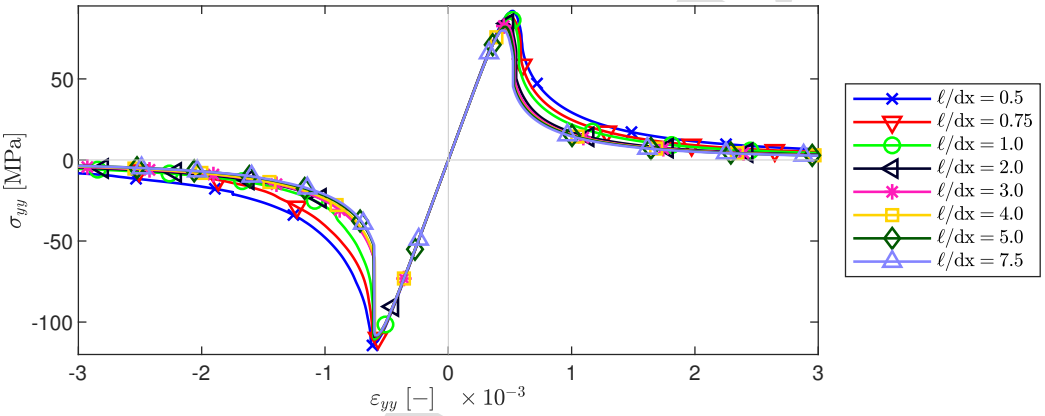

Figure 3: Effect of element size on load-displacement behaviour under compression (negative ε_{yy}) and tension (positive ε_{yy}).

for both cases at the sides of the hole. For the tensile cases, these cracks will propagate horizontally, whereas for the compression cases they will follow the direction of the maximum shear stress, propagating at an approximate 45° angle.

4.1.1. Element-size requirements

The guidance when using standard phase-field methods is to use $2-5$ elements per phase-field length scale. To confirm this still holds for the presented method, compression and tension simulations are performed for a range of element sizes, shown in Fig. 3. When the element size is larger than the phase-field length scale, this element size dictates the region over which the fracture energy is distributed, causing a more ductile behaviour. Starting from $\ell/\mathrm{dx} \approx 2$, similar behaviour is observed for both tension and compression, with further mesh refinement having an almost negligible effect, especially for the compressive cases. The near-overlapping curves for $\ell/\mathrm{dx} \geq 2$ in Fig. 3 are therefore the intended indication of mesh-independent behaviour, rather than a lack of resolution in the figure. The full mesh-refinement study is summarized by the load-displacement curves, while the displacement and phase-field contour plots are shown for representative coarse and refined meshes to illustrate the corresponding localization behaviour.

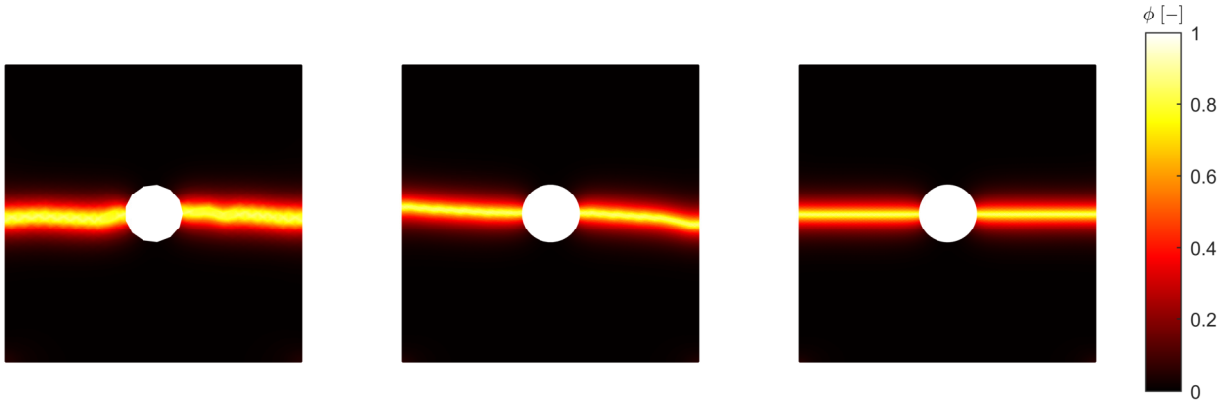

(a) $\ell/\mathrm{dx} = 1$ (b) $\ell/\mathrm{dx} = 3$ (c) $\ell/\mathrm{dx} = 5$

Figure 4: Effect of element size on phase field for the tensile plate with hole case. Results shown at an applied strain of $\varepsilon_{yy} = 3 \cdot 10^{-3}$.

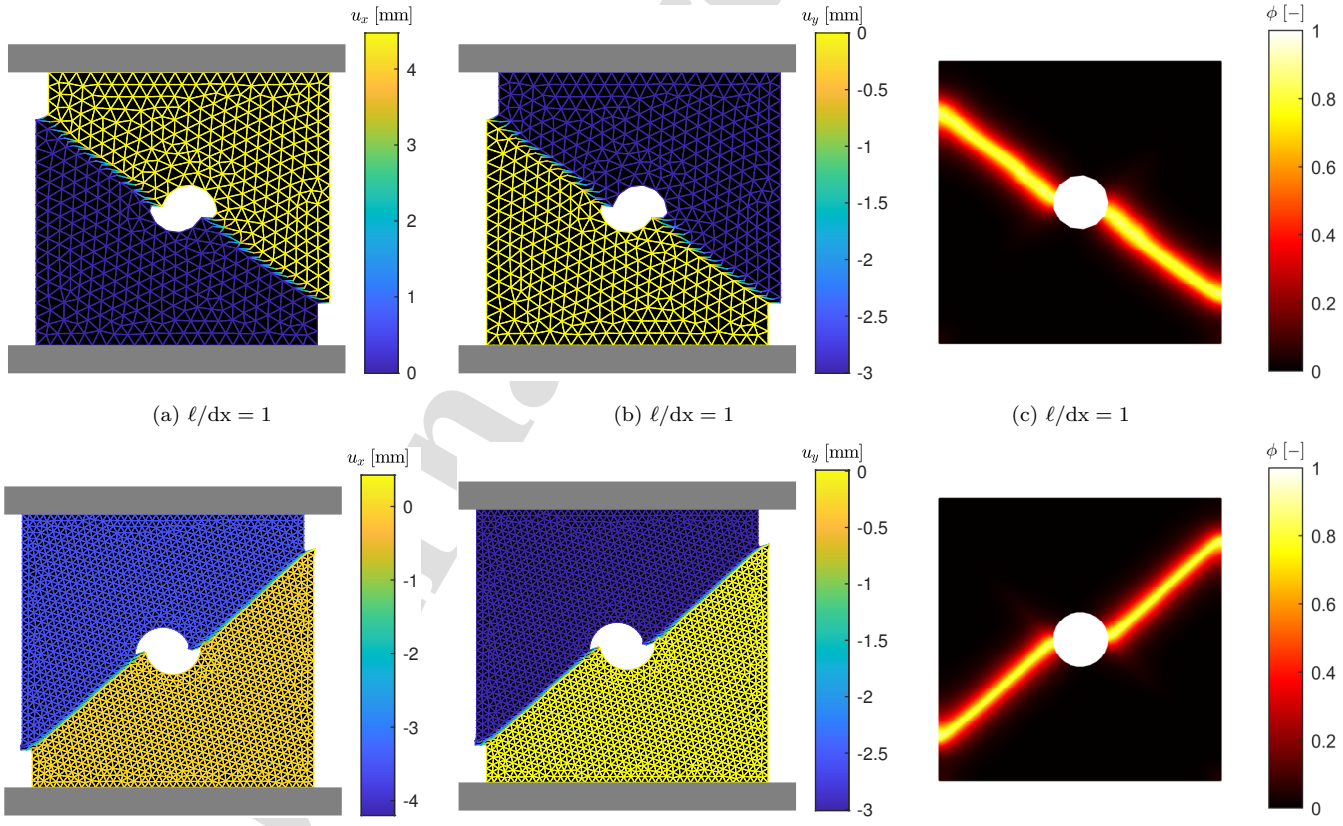

(a) $\ell/\mathrm{dx} = 1$ (b) $\ell/\mathrm{dx} = 1$ (c) $\ell/\mathrm{dx} = 1$

(d) $\ell/\mathrm{dx} = 2$ (e) $\ell/\mathrm{dx} = 2$ (f) $\ell/\mathrm{dx} = 2$

Figure 5: Horizontal (a,d) and vertical (b,e) displacement, with deformations magnified by ×10 and showing the elements, and phase-field variable (c,f) for the compressive plate-with-hole case, using a coarse and a finer mesh.

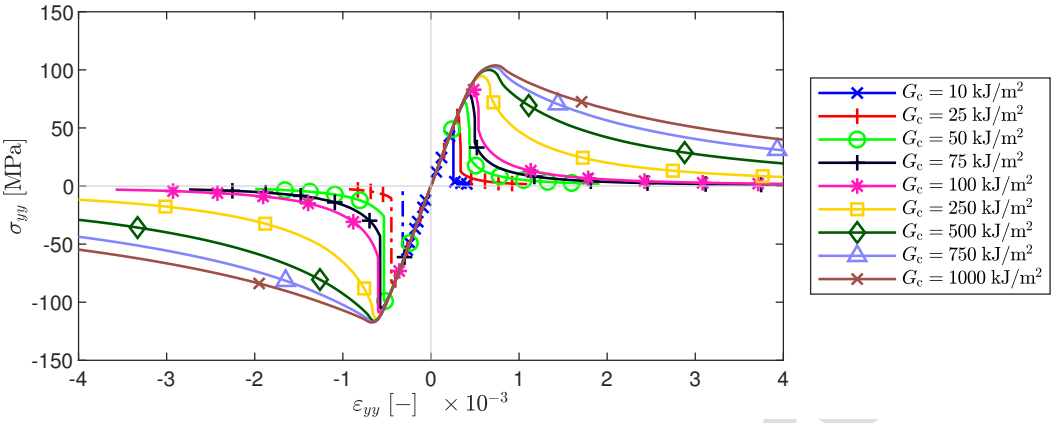

Figure 6: Effect of the fracture release energy G_c on the load-displacement behaviour for the tensile and compressive plate with hole cases. Cases using dashed lines correspond to the horizontal failure mode discussed in the text.

The phase-field obtained for the extensional case, shown in Fig. 4 confirm this mesh dependence: When using $\ell/\mathrm{dx} = 1$ a clear effect of element orientation and size is observed, with the phase-field following the orientation of the elements, causing a sawtooth-like crack. Upon mesh refinement, this pattern disappears and a smooth phase-field is obtained starting from $\ell/\mathrm{dx} = 3$. However, the crack still shows a minor influence of the element orientation, observed by the crack not being horizontal, up to $\ell/\mathrm{dx} = 5$ where a horizontal crack is obtained.

If we consider the compressive cases, Fig. 5, this element-orientation dependence is not exhibited as the crack path matches the element orientation, with $\ell/\mathrm{dx} = 2$ being sufficient to obtain mesh-independent results. Notably, displacement jump shows a clear localization to a single row of elements, and hence the thickness of the band over which the displacement jump is distributed becomes smaller with mesh refinement. However, the use of the phase-field distribution function to distribute the fracture release energy over a finite area suffices to regularize the problem and allow mesh-independent load-displacement behaviour to be obtained despite the displacement jump remaining localized. This case also shows that, for compressive cases, the fracture criterion correctly enforces a no-penetration condition, with the upper half of the domain slipping along the crack surface.

4.1.2. Fracture release energy

Next, we consider the effect of the fracture release energy, showing that the presented scheme correctly captures both the brittle behaviour expected at low energies, and the cohesive behaviour typical of higher fracture release energies. Simulations were performed for a range of energies between $G_c = 10$ kJ/m^2 and $G_c = 1000$ kJ/m^2, using a constant phase-field length scale of $\ell = 0.05$ m and characteristic element size $\ell/\mathrm{dx} = 3$. As in the mesh-refinement study, the full parameter sweep is summarized through the load-displacement curves, while contour plots are provided for the cases where the fracture pattern requires additional interpretation.

The resulting load-displacement behaviour, shown in Fig. 6, shows the clear impact of the fracture release energy. At low energies, an instantaneous drop in load is observed at the onset of fractures. As the energy is increased, this drop is reduced, and a more gradual unloading is observed, confirming that the model is able to correctly capture both the brittle and the cohesive regimes. For the lowest fracture energy under tension, where the behaviour is most brittle and the cohesive zone is negligible, the peak load can be compared to an analytical estimate. The

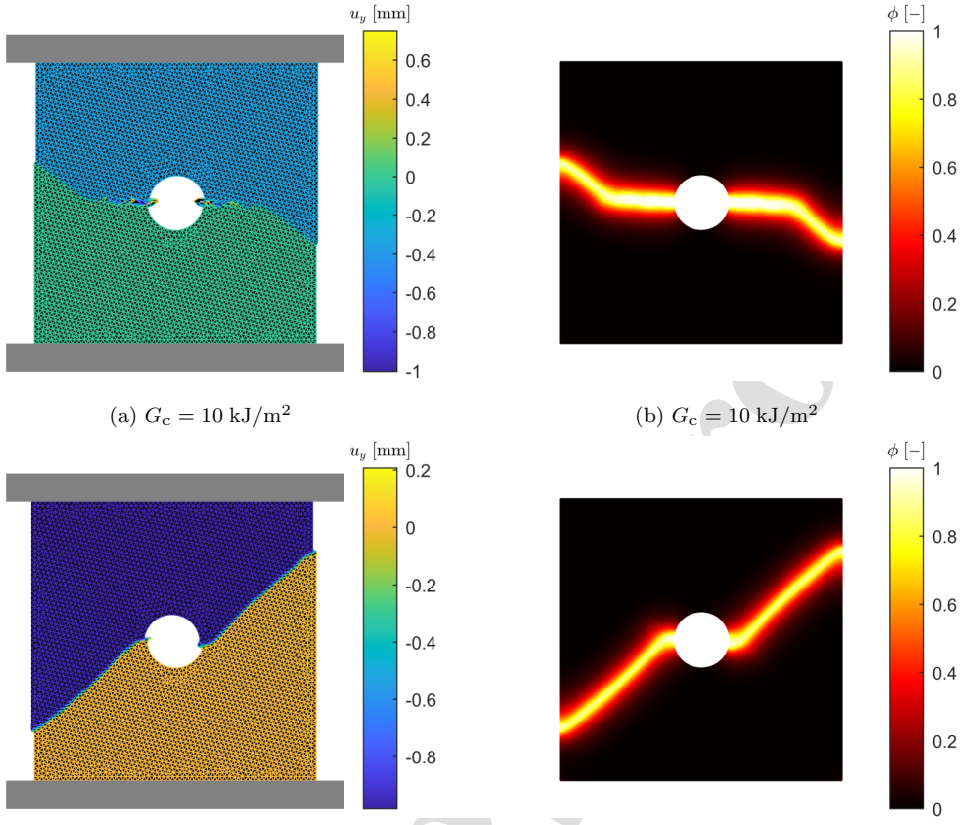

(a) $G_c = 10$ kJ/m^2 (b) $G_c = 10$ kJ/m^2

(c) $G_c = 25$ kJ/m^2 (d) $G_c = 25$ kJ/m^2

Figure 7: Vertical displacement (a,c) with deformations magnified by $\times 10$ and showing the elements, and phase-field variable (b,d) for the cases with low fracture release energy.

stress concentration factor for a circular hole in an infinite plate under uniaxial tension is $K_t = 3$ [50], such that the expected applied stress at crack nucleation is $\sigma_{nuc} \approx f_t/K_t = 50$ MPa. This is in agreement with the numerically obtained peak stress for the most brittle case in Fig. 6, confirming that the prescribed strength surface correctly governs the onset of fracture. We further note that an increased peak load is observed for the higher values of G_c, which is a consequence of the cohesion: when the fracture energy is low, the material fails as soon as the strength surface is reached, causing a sharp crack to propagate. While the stresses are still bounded by the failure surface for the higher values of G_c, the cohesive zone behind the crack tip allows the total load transferred to increase as the crack propagates, while also reducing the stress concentration at the crack tip. As a result, the total load transferred increases initially as the crack propagates, causing the increased strength observed for higher values of G_c.

The consistency between the crack-nucleation site and the onset of phase-field damage follows directly from the local constitutive update. Fracture eigenstrains, and therefore the crack-driving history field $\mathcal{F}$ used in the phase-field equation, can only develop at integration points where the stress state reaches the prescribed strength surface. In the tensile plate-with-hole case this occurs first at the sides of the hole, where the elastic stress concentration is largest. The agreement between the computed peak stress and $\sigma_{nuc} \approx f_t/K_t$ therefore confirms that crack nucleation is governed by the strength surface, rather than by the phase-field length scale or fracture energy.

This transition can be understood by noting that the strength surface controls crack nucleation, while G_c controls the energy required to open and propagate a cohesive crack. Changing G_c changes the post-initiation cohesive response: low G_c corresponds to a small amount of energy dissipation and a short cohesive/process zone, so the material rapidly loses its load-carrying capacity once the strength surface is reached. Higher G_c requires more energy to be dissipated during crack opening, increasing the characteristic cohesive length scale and allowing cohesive tractions to continue being transferred behind the crack tip. A useful estimate for this length is $l_{ch} \approx EG_c/(1-\nu^2)/f_t^2$ for plane strain. Using the material parameters from Table 1, this gives $l_{ch} \approx 0.1$ m for $G_c = 10$ kJ/m^2, which is much smaller than the 1 m specimen width, and $l_{ch} \approx 10$ m for $G_c = 1000$ kJ/m^2, which is larger than the simulated domain. The lowest-energy cases therefore behave close to a brittle crack, whereas at the highest energies the complete crack path remains within the cohesive/process-zone scale, explaining the gradual unloading and increased apparent load capacity. These results furthermore confirm that the model correctly decouples the physical length scale, introduced through the tensile strength and fracture release energy, from the numerical length scale, introduced through the phase-field length scale.

However, even though the load-displacement behaviour of all cases looks plausible, under compression the two cases with the lowest fracture release energy, $G_c = 10$ kJ/m^2 and $G_c = 25$ kJ/m^2, showed a different failure mode where the phase field did not localize into a diagonal shear band from the onset. Instead, cracks initially propagated horizontally with the phase-field spreading over a region roughly twice the width of properly localized cracks, as shown in Fig. 7. The displacements obtained within these two cases also show a clearly different behaviour, where the material is crushed/squeezed horizontally, rather than slipping along a diagonal crack. As this horizontal damage zone propagates sideways, it eventually localizes into diagonal cracks. This behaviour was verified to be consistent across time-step refinements, phase-field length scales, staggered iteration counts, and both failure criteria considered, confirming that it is not a numerical artefact. A plausible explanation follows from the stress distribution around a circular hole under far-field compression [50]: a tensile hoop stress develops at the sides of the hole that decays rapidly with distance, alongside the far-field shear stress that sustains diagonal shear bands. At low G_c, the cohesive zone is negligible and the horizontal mode-I crack, driven by this tensile hoop stress, can propagate over a significant distance before the diminishing driving force arrests it. At higher G_c, the cohesive zone resistance arrests the horizontal crack after only short propagation, leaving the diagonal shear band, sustained by the far-field stress state, as the dominant mode. This competition between crack modes is only observed under compression, where both tensile hoop stresses and shear stresses coexist, and not under tension, where the stress state unambiguously drives a horizontal mode-I crack.

4.1.3. Length-scale dependence

Finally, we consider the effect of the phase-field length scale ℓ, showing that within the presented model this is solely an indicator of the width of the phase-field region, rather than impacting the physical behaviour. Simulations were performed for a range of length scales between $\ell = 0.01$ m and $\ell = 0.1$ m. These simulations were performed with a constant fracture release energy of $G_c = 100$ kJ/m^2 and characteristic element size $\ell/\mathrm{dx} = 3$. The resulting load displacement behaviour, Fig. 8, confirms that the phase-field length scale has negligible effect on the strength and energy dissipation during fracture. An order of magnitude difference in length scale (and element size) results

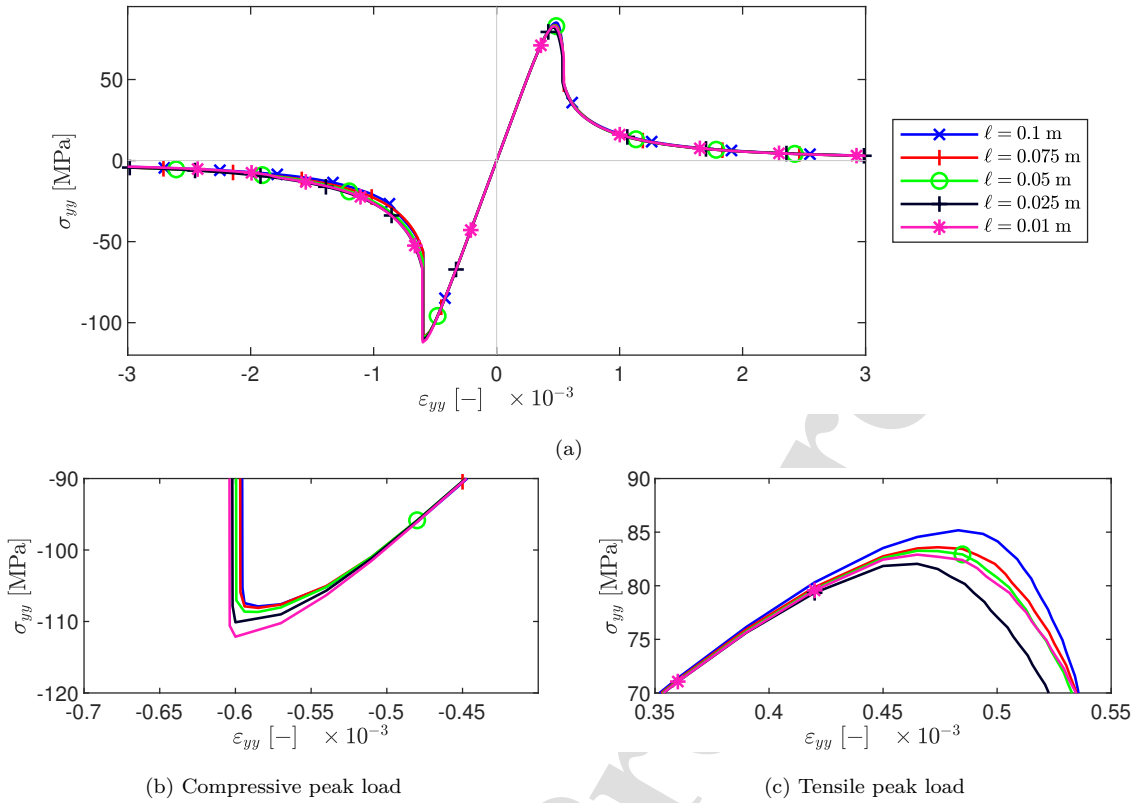

Figure 8: Effect of phase-field length scale on the load-displacement behaviour, and zooms on relevant regions.

in less than 5% difference in the obtained peak load. While the unloading behaviour, especially for the compression cases, shows a slightly larger difference, with smaller length-scales experiencing a reduced drop in stress at the onset of fracture, this is still relatively minor and can be attributed to the reduced element size aiding with the localization of cracks and better resolving the increased stress concentrations.

The obtained phase-field solutions and displacements, shown in Fig. 9, confirm that the length scale only impacts the width of the phase-field region. For both cases, the actual displacement discontinuity is limited to a single row of elements, despite the phase-field being distributed over a wider region for the larger length scales. Notably, even though the largest length scale is comparable to the size of the hole, it still localized properly to the sides of the hole, showing that as the phase-field is driven by the fracture-eigenstrains, it is able to localize to the correct regions even when the length scale is large. One notable effect of the length scale is on the computational cost, with the finest length scale requiring 100× more elements than the coarsest length scale, and thus a significantly increased computational time (close to a day for $\ell = 0.01$ m compared to around 5 min for $\ell = 0.1$ m). This highlights the implications of having the length scale decoupled from the material strength: allowing for a length scale that is as large as possible to limit the computational cost of simulations, with the main restrictions following from the details of the features that are being resolved, while still obtaining the same crack paths and behaviour as would be obtained through fine length-scale simulations.

To more clearly convey this decoupling, Fig. 10 compares the cohesive phase-field model with conventional AT-1 and AT-2 phase-field models for the tensile plate-with-hole case. The comparison is restricted to tension so that

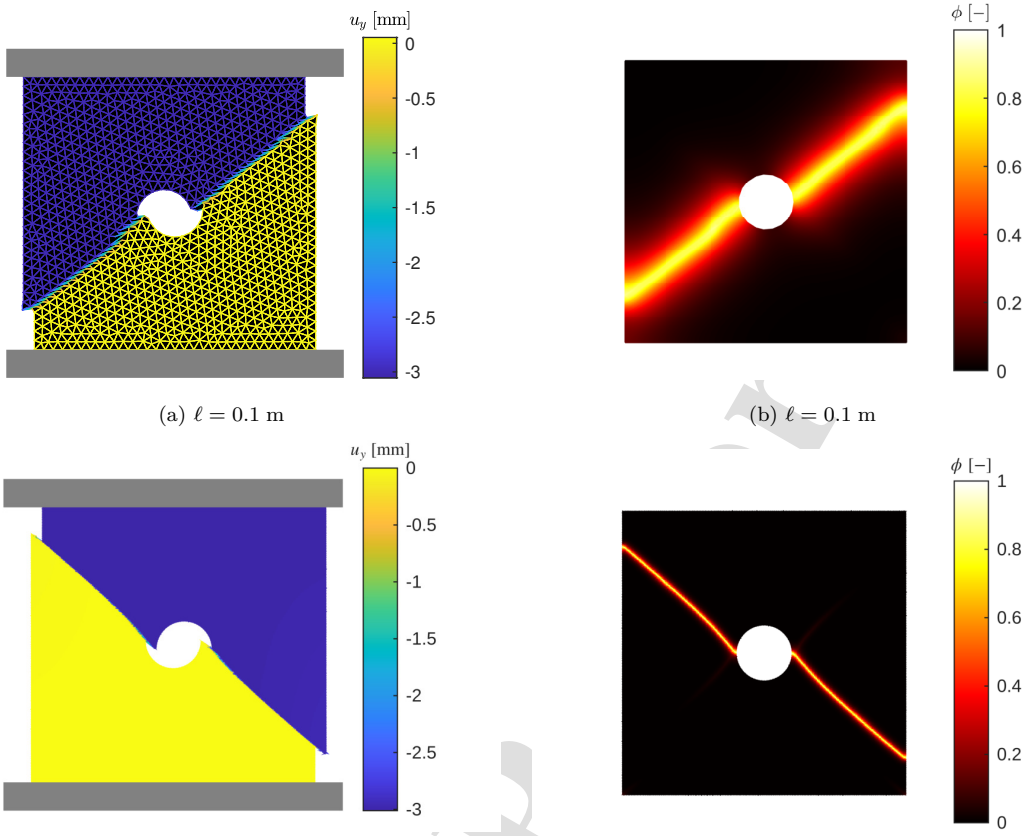

(a) $\ell = 0.1$ m (b) $\ell = 0.1$ m

(c) $\ell = 0.01$ m (d) $\ell = 0.01$ m

Figure 9: Vertical displacements (a,c, deformations magnified by $\times 10$) and phase-field (b,d) obtained for applied strains of $\varepsilon = 3 \cdot 10^{-3}$, using different phase-field length scales.

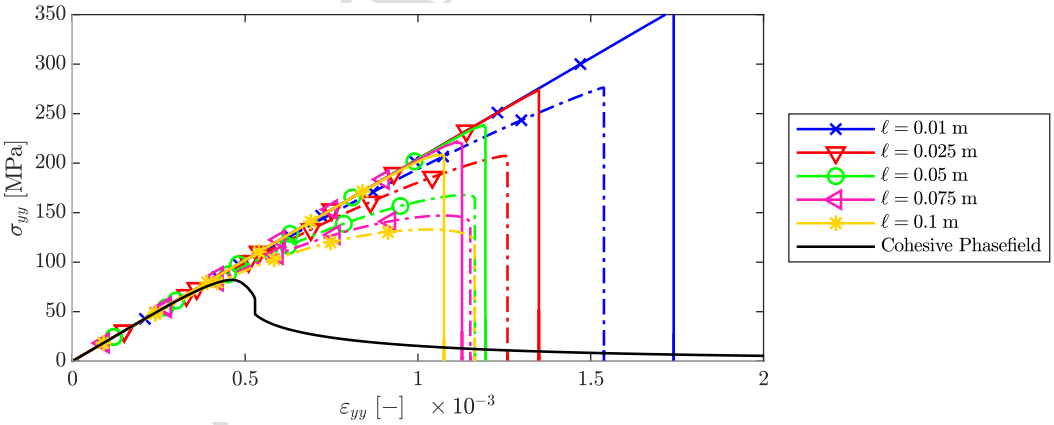

Figure 10: Comparison between the cohesive phase-field model (solid black line) and traditional AT-1 and AT-2 phase-field models (solid and dashed coloured lines) for the tensile plate-with-hole case with $G_c = 100$ kJ/m^2. The coloured curves show the length-scale sensitivity of the apparent strength in AT-1 and AT-2 when G_c is kept fixed.

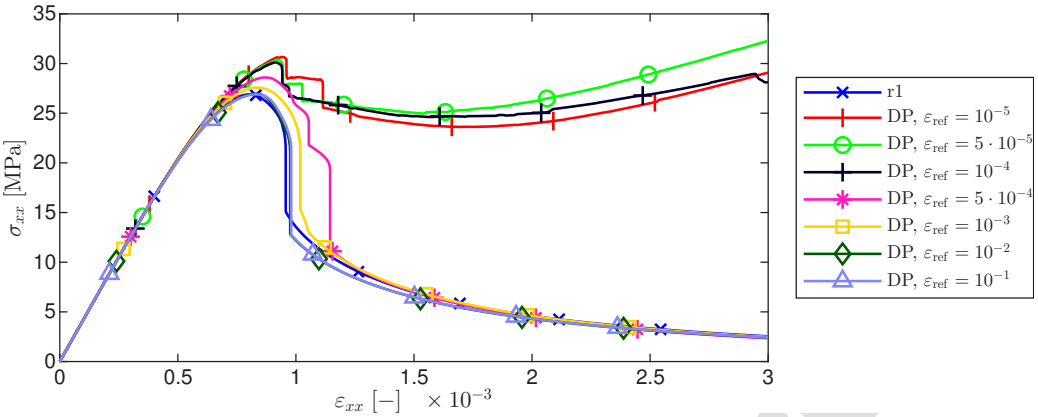

Figure 11: Load-displacement behaviour of the single-edge notched plate under shear loading, using the $r1$ and Drucker-Prager-like (referred to as "DP") strength criteria, for a range of reference strains. The sudden load drops identify the shear-dominated regime, while the smoother hardening-like responses correspond to tensile/mixed-mode propagation, with intermediate curves representing the transition between these limits.

differences in compressive/tensile driving-force splits do not affect the interpretation. In the cohesive formulation, f_{t} and G_{c} are prescribed independently of the numerical phase-field length scale, and the response in Fig. 8 remains nearly unchanged when ℓ is varied. In conventional AT-1 and AT-2 models, by contrast, crack nucleation is tied to the regularization length: for the homogeneous one-dimensional response the apparent tensile strengths are $f_{\text{t}} = \sqrt{3G_{\text{c}}E/(8\ell)}$ and $f_{\text{t}} = \sqrt{27G_{\text{c}}E/(256\ell)}$, respectively. With the material parameters from Table 1 and $G_{\text{c}} = 100$ kJ/m^2, matching the prescribed tensile strength $f_{\text{t}} = 150$ MPa would require $\ell \approx 0.33$ m for AT-1 and $\ell \approx 0.094$ m for AT-2. For the present geometry, the AT-1 value is larger than the hole diameter, while the AT-2 value is comparable to the hole radius and to the largest length scale considered in the length-scale study. These values are therefore dictated by strength calibration rather than by the geometric resolution of the crack path: choosing a smaller ℓ to localize the crack more sharply necessarily increases the apparent nucleation strength, while choosing the strength-matching ℓ fixes the width of the regularized damage zone. The proposed cohesive formulation avoids this trade-off by using ℓ only to regularize the phase-field distribution, while the strength surface and G_{c} control crack nucleation and propagation separately.

4.2. Single-edge notched plate

Next, we consider a single-edge notched plate under shear loading, shown in Fig. 2(b). The bottom of the domain is fixed in horizontal and vertical directions, the top surface is fixed in vertical direction while a horizontal displacement is imposed at a rate of $\dot{U}_{\text{Shear}} = 1 \cdot 10^{-6}$ m/s. Due to the stress concentration at the tip of the notch, a crack will form at this location. If fracture is driven by the shear stresses, the crack will propagate horizontally, while if it is driven by tensile stresses, the crack will propagate downwards under an approximate 45° angle. Mixed-mode fracture will result in a fracture path in between these two extreme cases. We will consider both the $r1$ strength criterion from Eq. (17) as well as the Drucker-Prager-like criterion from Eq. (18) with varying reference strains ε_{ref}, controlling the increased strength in the compressive regime.

The resulting load-displacement behaviour, shown in Fig. 11, indicates two distinct regimes for crack propagation: Using the $r1$ criterion or the Drucker-Prager-like criterion with a high reference strain, a sudden drop in load is

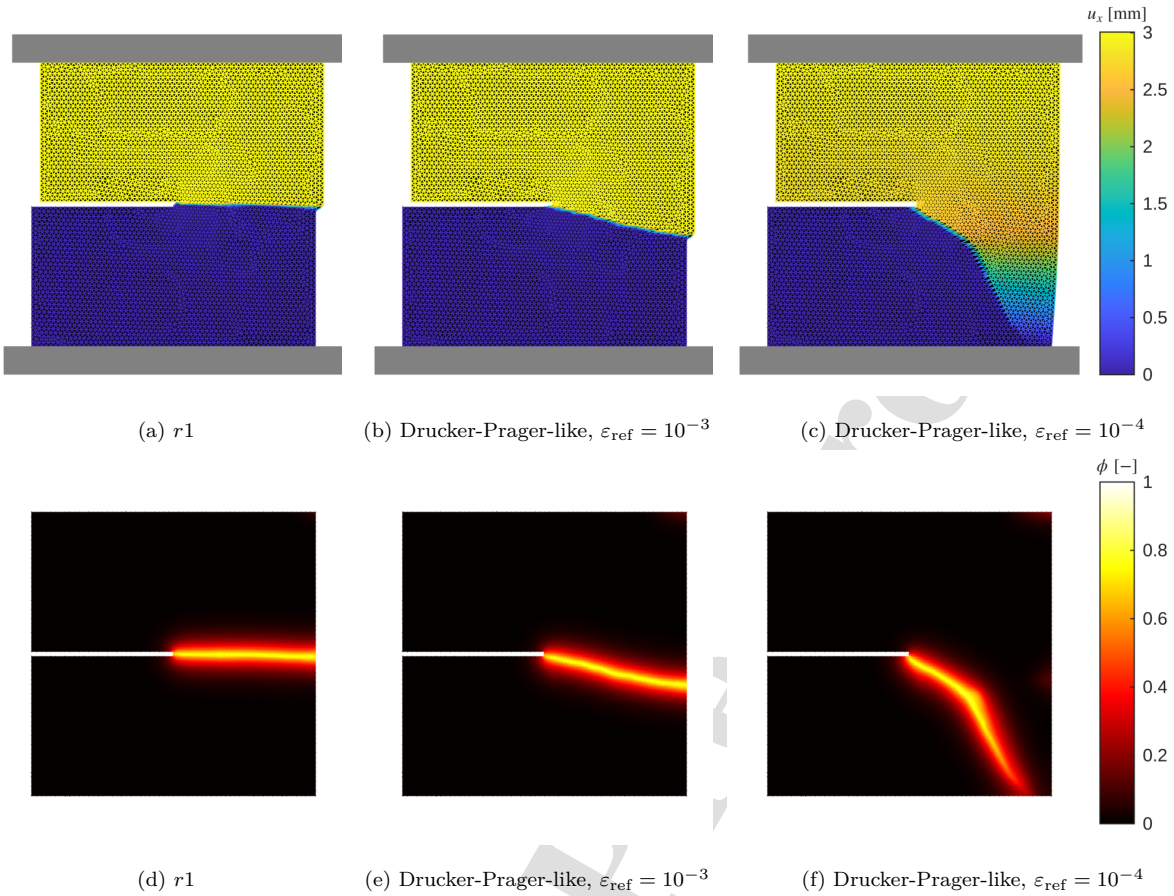

(a) $r1$ (b) Drucker-Prager-like, $\varepsilon_{\text{ref}} = 10^{-3}$ (c) Drucker-Prager-like, $\varepsilon_{\text{ref}} = 10^{-4}$

(d) $r1$ (e) Drucker-Prager-like, $\varepsilon_{\text{ref}} = 10^{-3}$ (f) Drucker-Prager-like, $\varepsilon_{\text{ref}} = 10^{-4}$

Figure 12: Horizontal displacements (a-c) and phase-field variable (d-f) obtained for the single-edge notched plate under shear loading at an applied strain of $\varepsilon_{xy} = 3 \cdot 10^{-3}$, using the $r1$ and Drucker-Prager-like strength criteria. Colourbars are shared across all three cases.

observed during crack propagation. Representative results for this regime are shown in Fig. 12(a,d), showing that the crack propagation is driven by shear. In contrast, using the Drucker-Prager-like criterion with a low reference strain, Fig. 12(c,f), and thus a higher shear strength in compressive regions, the shear crack is partially suppressed with the initial crack propagating in a mixed-mode manner, before switching to a mode-I crack only. This competition between shear and tensile crack propagation is also observed in the load-displacement behaviour, showing small drops in strength during the mixed-mode propagation, while showing a hardening-like behaviour during later propagation, where the crack is driven by tensile stresses only. The intermediate cases are therefore interpreted as a transition between the shear-dominated and tensile/mixed-mode regimes, rather than as a separate third failure mechanism.

Notably, all cracks propagate either horizontally or downwards, with none of the cases showing cracks propagating upwards. This is a consequence of the crack driving force expressions: The r1 expression from Eq. (17) explicitly removing compressive strains from the driving force by putting these in a non-damaged term, F_{i}, such that mode-I cracks are solely driven by extensional stresses. The resulting driving force in the compressive regime is solely due to deviatoric stresses, hence causing horizontal crack propagation. For the Drucker-Prager-like criterion, Eq. (18),

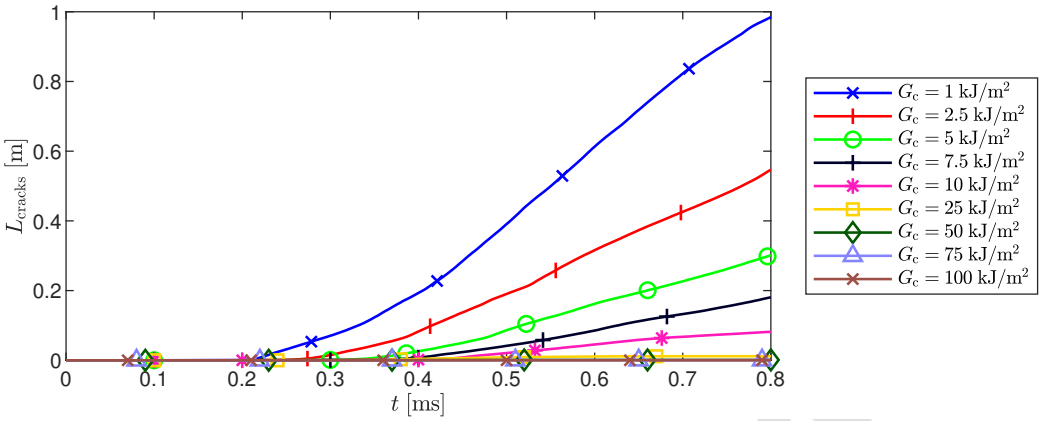

Figure 13: Impact of fracture energy release rate G_c on the combined crack length for the dynamic fracture case.

volumetric strains do not contribute to crack propagation as they are not aligned with the eigenstrain directions under compressive loading via the direction $\mathbf{G}$. While the approaches to eliminate the contribution of compressive stresses to crack propagation differ between the two criteria, they both successfully achieve this, resulting in no cracks propagating upwards.

4.3. Dynamic fracture

The final case considered consists of a notched plate of 1 m $\times$ 0.5 m with an initial notch of 0.25 m at the centre-left edge, shown in Fig. 2(c). An external traction of $\sigma_{\text{ext}} = 10$ MPa is applied to the top and bottom edges. As this case considers the dynamic behaviour, we set the damping coefficient to $c = 0$. To give a detailed look into the crack paths, we also use a smaller phase-field length scale of $\ell = 0.01$ m, with a corresponding element size of $\mathrm{dx} = \ell/3$. The fracture criterion uses the Drucker-Prager-like criterion from Eq. (18) with a reference strain of $\varepsilon_{\text{ref}} = 1$, practically removing the pressure dependence while retaining the smooth transition between mode-I and mode-II cracks. The fracture release energy G_c is varied between 1 kJ/m^2 and 100 kJ/m^2, covering purely brittle crack propagation to a more cohesive behaviour. To get a measure of the length of the developed cracks, we estimate the total crack length through the phase-field distribution function γ, Eq. (4), as:

$$L_{\text{crack}} \approx \int_{\Omega} \gamma(\phi)\, \mathrm{d}\Omega \tag{31}$$

where we note that this only gives an estimate of the crack length for ductile cases. This is due to the phase-field distribution function being defined as the degradation of the fracture energy, rather than the presence of cracks as in standard phase-field methods. Hence, when the material has a noticeable cohesive zone, where $\phi < 1$ along the crack, the obtained length will be an underestimate of the actual crack length. For brittle cases, where the phase-field is $\phi \approx 1$ along the crack, this estimate is more accurate.

The evolution of the crack length over time is shown in Fig. 13. As expected, the cases with the lowest fracture release energy have the fastest crack propagation, reaching the edges of the domain after 0.8 ms. Increasing the value of the fracture energy reduces the rate of crack propagation, with the $G_c = 10$ kJ/m^2 case showing approximately 10% of the crack length of the $G_c = 1$ kJ/m^2 case. The curves for the higher fracture energies remain close to the horizontal axis because these cases do not develop measurable crack propagation over the simulated time

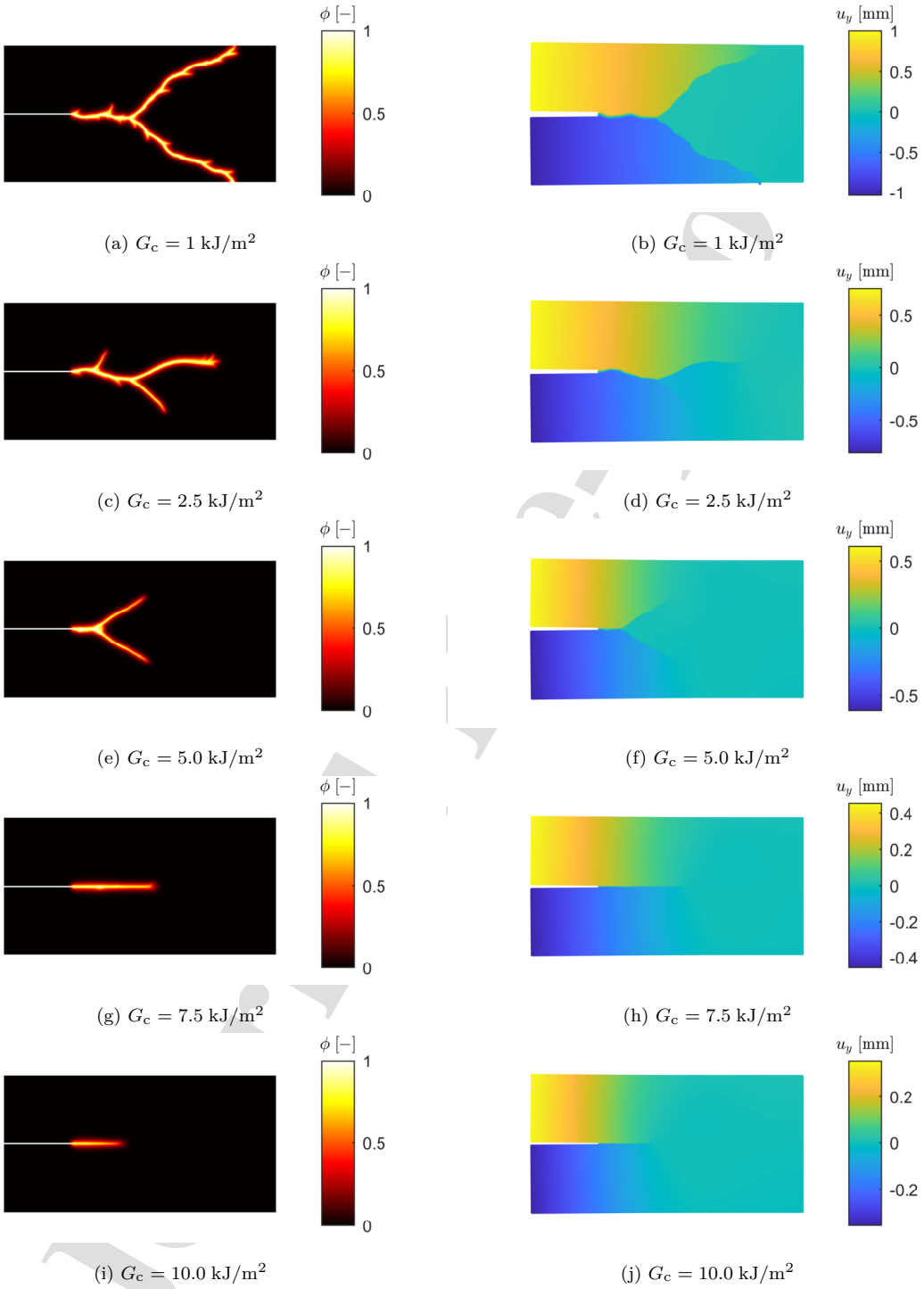

(a) $G_c = 1$ kJ/m^2 (b) $G_c = 1$ kJ/m^2

(c) $G_c = 2.5$ kJ/m^2 (d) $G_c = 2.5$ kJ/m^2

(e) $G_c = 5.0$ kJ/m^2 (f) $G_c = 5.0$ kJ/m^2

(g) $G_c = 7.5$ kJ/m^2 (h) $G_c = 7.5$ kJ/m^2

(i) $G_c = 10.0$ kJ/m^2 (j) $G_c = 10.0$ kJ/m^2

Figure 14: Phase-field (left column) and vertical displacement (right column, magnified by $\times 1000$) obtained for the dynamic fracture case at $t = 0.8$ ms.

interval. The obtained fracture pattern for the $G_c = 1$ kJ/m^2 case is shown in Fig. 14(a,b), showing the crack develops short branches as it propagates to dissipate additional energy, and branches into two distinct cracks. As the fracture release energy is increased, Fig. 14(c,d), the formation of distinct branches is suppressed, with the branches that develop halting their propagation soon after forming. Higher values for G_c suppress these unstable branches, creating two distinct crack branches without additional bifurcations, Fig. 14(e,f). Further increases to the fracture release energy, Fig. 14(g,h) and Fig. 14(i,j) fully suppress all crack branching, resulting in a single crack propagating horizontally from the initial notch. As the fracture energy is increased beyond $G_c = 10$ kJ/m^2, the fracture becomes unable to propagate, instead creating a small region at the crack tip where the phase-field is increased.

The connection between G_c and branching follows from the dynamic energy balance. In the present formulation, the fracture dissipation rate is

$$\dot{\Psi}_c = G_c \int_\Omega \dot{\gamma}(\phi)\, \mathrm{d}\Omega \approx G_c \dot{L}_{\mathrm{crack}}. \tag{32}$$

A bifurcating crack therefore dissipates more elastic energy than a single straight crack, since multiple crack tips create additional crack length over the same time interval. For low G_c, the energetic cost of this additional crack surface is small relative to the elastic and kinetic energy released by the rapidly propagating crack, so off-axis branches can form as an additional dissipation mechanism. At $G_c = 5$ kJ/m^2, the available driving energy is close to this transition: a secondary branch initiates and grows, but further bifurcation is suppressed. For higher G_c, a larger fraction of the available energy is spent extending the main cohesive crack and maintaining the cohesive zone, which reduces both the crack speed and the off-axis driving force. No additional branches are formed for these higher G_c cases, and the solution evolves towards a single horizontal crack.

The asymmetry of the damage zones in Fig. 14 follows from this same dynamic branching instability. Once an off-axis branch initiates, the elastic and kinetic energy available near the crack tip is redistributed between competing crack paths. In the transitional cases, there is sufficient energy for a secondary branch to nucleate, but not for both branches to develop into self-sustaining cracks. Small perturbations from the discretization, time integration, and nonlinear solution procedure therefore select one branch, which continues to grow and shields the opposing branch, causing it to stagnate. The direction of this symmetry breaking is not prescribed by the model, similar to the diagonal crack direction selected in the compressed plate-with-hole case. The full specimen is simulated here, rather than imposing a symmetry boundary condition, so asymmetric branching is not artificially suppressed.

We note that all the cases use the same strength surface, using the same values for the tensile and shear strength, hence showing that these do not play a significant role in determining when cracks can propagate. This is in contrast to the previous cases that studied crack initialization, where the strength surface and tensile strength played a dominant role. As a result, this indicates that the presented scheme correctly captures the physical behaviour of crack nucleation and propagation, with the strength surface governing the former and the fracture release energy governing the latter, with both of these aspects being independent of the phase-field length scale used for the numerical regularization.

5. Conclusions

In this paper, we presented a computational framework for modelling cohesive fractures within the phase-field fracture paradigm. The main contribution is the return-mapping reformulation of an eigenstrain-based cohesive phase-field model with an explicit strength surface, which turns the additional fracture-eigenstrain fields of previous energy-minimization formulations into an integration-point-local constitutive update. This is significant because it allows strength-controlled crack nucleation and energy-controlled cohesive propagation to be introduced into standard finite-element phase-field implementations without additional global eigenstrain degrees of freedom. Using the concept of fracture eigenstrains from [35] and integrating this within a local constitutive model, we are able to capture both brittle and cohesive fracture nucleation and propagation. The presented method is able to use a strength surface to predict the stress required for fracture nucleation, while the energy release rate governs the propagation behaviour. Furthermore, due to the used local formulation, no additional degrees of freedom are required to capture the cohesive behaviour compared to standard phase-field formulations, with the complete cohesive behaviour solved on a per-integration-point basis comparable to plasticity models. As a result, the presented model is straightforward to integrate within existing codes, and an example implementation is provided (see data availability statement).

The three benchmark cases confirm that crack nucleation is governed by the prescribed strength surface, while propagation is controlled by the fracture energy release rate G_c, with both aspects independent of the phase-field length scale ℓ. Specifically, varying ℓ over an order of magnitude (from 0.01 m to 0.1 m) produced less than 5% variation in peak load for both tension and compression. The element-size study showed that mesh-independent load-displacement responses are obtained for $\ell/\mathrm{dx} \geq 2$, consistent with the guidance for standard phase-field methods. For the dynamic branching case, reducing G_c from 10 kJ/m^2 to 1 kJ/m^2 increased the crack length by approximately an order of magnitude and triggered crack branching, demonstrating the model's ability to capture complex fracture phenomena without ad-hoc criteria. Within this benchmark setting, the results demonstrate that the return-mapping formulation provides a practical route for introducing explicit strength surfaces and cohesive fracture behaviour into standard finite-element phase-field implementations. The conclusions are limited to the homogeneous, small-strain problems considered: applying the same local-update structure to nonlinear material behaviour, finite strains, heterogeneity, or interfaces would require additional constitutive choices beyond those addressed in this manuscript.

Data availability

The finite element code used within this study, together with all input files required to reproduce the results presented in this paper, is available at `https://github.com/T-Hageman/Cohesive-PhaseField-FenicsX`.

Acknowledgements

No external funding was received for this research.

Declaration of competing interest

The author declares that they have no known competing financial interests or personal relationships that could have appeared to influence the work reported in this paper.

CRediT authorship contribution statement

Tim Hageman: Conceptualization, Methodology, Software, Validation, Formal analysis, Investigation, Data curation, Writing - original draft, Visualization.

Declaration of generative AI in the writing process

During the preparation of this manuscript, the author used GitHub Copilot (Claude, Anthropic) to assist with improving the language and readability of the text, and provide critical feedback on draft versions. The author reviewed and edited all AI-generated suggestions and takes full responsibility for the content of the published work.

References

[1] A. Egger, U. Pillai, K. Agathos, E. Kakouris, E. Chatzi, I. A. Aschroft, S. P. Triantafyllou, Discrete and phase field methods for linear elastic fracture mechanics: A comparative study and state-of-the-art review, Applied Sciences 9 (12) (2019) 2436. doi:10.3390/app9122436.

[2] R. de Borst, Fracture and damage in quasi-brittle materials: A comparison of approaches, Theoretical and Applied Fracture Mechanics 122 (2022) 103652. doi:10.1016/j.tafmec.2022.103652.

[3] Y. Navidtehrani, C. Betegón, E. Martínez-Pañeda, A simple and robust Abaqus implementation of the phase field fracture method, Applications in Engineering Science 6 (2021) 100050. doi:10.1016/j.apples.2021.100050.

[4] W.-X. Chen, J.-Y. Wu, Phase-field cohesive zone modeling of multi-physical fracture in solids and the open-source implementation in Comsol Multiphysics, Theoretical and Applied Fracture Mechanics 117 (2022) 103153. doi:10.1016/j.tafmec.2021.103153.

[5] G. Molnár, A. Gravouil, 2D and 3D Abaqus implementation of a robust staggered phase-field solution for modeling brittle fracture, Finite Elements in Analysis and Design 130 (2017) 27–38. doi:10.1016/j.finel.2017.03.002.

[6] B. Bourdin, J.-J. Marigo, C. Maurini, P. Sicsic, Morphogenesis and propagation of complex cracks induced by thermal shocks, Physical Review Letters 112 (1) (2014) 014301. doi:10.1103/PhysRevLett.112.014301.

[7] M. Hofacker, C. Miehe, A phase field model of dynamic fracture: Robust field updates for the analysis of complex crack patterns, International Journal for Numerical Methods in Engineering 93 (3) (2013) 276–301. doi:10.1002/nme.4387.

[8] M. F. Wheeler, T. Wick, W. Wollner, An augmented-Lagrangian method for the phase-field approach for pressurized fractures, Computer Methods in Applied Mechanics and Engineering 271 (2014) 69–85. doi:10.1016/j.cma.2013.12.005.

[9] T. Clayton, R. Duddu, T. Hageman, E. Martínez-Pañeda, Modeling ice cliff stability using a new Mohr–Coulomb-based phase field fracture model, Journal of Glaciology 71 (2025) e70. doi:10.1017/jog.2025.21.

[10] X. Sun, R. Duddu, Hirshikesh, A poro-damage phase field model for hydrofracturing of glacier crevasses, Extreme Mechanics Letters 45 (2021) 101277. doi:10.1016/j.eml.2021.101277.

[11] C. Miehe, S. Mauthe, S. Teichtmeister, Minimization principles for the coupled problem of Darcy–Biot-type fluid transport in porous media linked to phase field modeling of fracture, Journal of the Mechanics and Physics of Solids 82 (2015) 186–217. doi:10.1016/j.jmps.2015.04.006.

[12] T. Wu, L. De Lorenzis, A phase-field approach to fracture coupled with diffusion, Computer Methods in Applied Mechanics and Engineering 312 (2016) 196–223. doi:10.1016/J.CMA.2016.05.024.

[13] F. P. Duda, A. Ciarbonetti, S. Toro, A. E. Huespe, A phase-field model for solute-assisted brittle fracture in elastic-plastic solids, International Journal of Plasticity 102 (2018) 16–40. doi:10.1016/J.IJPLAS.2017.11.004.

[14] T. Hageman, E. Martínez-Pañeda, A phase field-based framework for electro-chemo-mechanical fracture: Crack-contained electrolytes, chemical reactions and stabilisation, Computer Methods in Applied Mechanics and Engineering 415 (2023) 116235. doi:10.1016/j.cma.2023.116235.

[15] T. K. Mandal, V. P. Nguyen, J. Y. Wu, Comparative study of phase-field damage models for hydrogen assisted cracking, Theoretical and Applied Fracture Mechanics 111 (2021) 102840. doi:10.1016/J.TAFMEC.2020.102840.

[16] P. K. Kristensen, C. F. Niordson, E. Martinez-Paneda, An assessment of phase field fracture: Crack initiation and growth, Philosophical Transactions of the Royal Society A 379 (2203) (2021) 20210021. doi:10.1098/RSTA.2021.0021.

[17] O. Lopez-Pamies, J. E. Dolbow, G. A. Francfort, C. J. Larsen, Classical variational phase-field models cannot predict fracture nucleation, Computer Methods in Applied Mechanics and Engineering 433 (2025) 117520. doi:10.1016/j.cma.2024.117520.

[18] A. A. Griffith, The phenomena of rupture and flow in solids, Philosophical Transactions of the Royal Society of London, Series A: Containing Papers of a Mathematical or Physical Character 221 (582-593) (1921) 163–198. doi:10.1098/rsta.1921.0006.

[19] E. Tanné, T. Li, B. Bourdin, J. J. Marigo, C. Maurini, Crack nucleation in variational phase-field models of brittle fracture, Journal of the Mechanics and Physics of Solids 110 (2018) 80–99. doi:10.1016/j.jmps.2017.09.006.

[20] T. K. Mandal, V. P. Nguyen, J.-Y. Wu, Length scale and mesh bias sensitivity of phase-field models for brittle and cohesive fracture, Engineering Fracture Mechanics 217 (2019) 106532. doi:10.1016/j.engfracmech.2019.106532.

[21] A. Kumar, B. Bourdin, G. A. Francfort, O. Lopez-Pamies, Revisiting nucleation in the phase-field approach to brittle fracture, Journal of the Mechanics and Physics of Solids 142 (2020) 104027. doi:10.1016/j.jmps.2020.104027.

[22] L. De Lorenzis, C. Maurini, Nucleation under multi-axial loading in variational phase-field models of brittle fracture, International Journal of Fracture (2021) 1–21doi:10.1007/s10704-021-00555-6.

[23] F. Vicentini, C. Zolesi, P. Carrara, C. Maurini, L. De Lorenzis, On the energy decomposition in variational phase-field models for brittle fracture under multi-axial stress states, International Journal of Fracture (Apr. 2024). doi:10.1007/s10704-024-00763-w.

[24] S. Zhang, W. Jiang, M. R. Tonks, Assessment of four strain energy decomposition methods for phase field fracture models using quasi-static and dynamic benchmark cases, Materials Theory 2022 6:1 6 (1) (2022) 1–24. doi:10.1186/S41313-021-00037-1.

[25] D. Infante-García, A. R. Quiñonero-Moya, M. Álvarez-Blanco, E. Giner, Verification of strain energy splits of phase field fracture model using Westergaard's problem under mixed-mode loading, Engineering Fracture Mechanics 308 (2024) 110371. doi:10.1016/j.engfracmech.2024.110371.

[26] R. J. M. Geelen, Y. Liu, T. Hu, M. R. Tupek, J. E. Dolbow, A phase-field formulation for dynamic cohesive fracture, Computer Methods in Applied Mechanics and Engineering 348 (2019) 680–711. doi:10.1016/j.cma.2019.01.026.

[27] A. Gupta, D. T. Nguyen, Hirshikesh, R. Duddu, Damage mechanics challenge: Predictions from an adaptive finite element implementation of the stress-based phase-field fracture model, Engineering Fracture Mechanics (2024) 110252doi:10.1016/j.engfracmech.2024.110252.

[28] Y. Feng, J. Li, A unified regularized variational cohesive fracture theory with directional energy decomposition, International Journal of Engineering Science 182 (2023) 103773. doi:10.1016/j.ijengsci.2022.103773.

[29] K. Pham, H. Amor, J.-J. Marigo, C. Maurini, Gradient damage models and their use to approximate brittle fracture, International Journal of Damage Mechanics 20 (4) (2011) 618–652. doi:10.1177/1056789510386852.

[30] C. V. Verhoosel, R. de Borst, A phase-field model for cohesive fracture, International Journal for Numerical Methods in Engineering 96 (1) (2013) 43–62. doi:10.1002/NME.4553.

[31] Y. Ghaffari Motlagh, R. de Borst, Considerations on a phase-field model for adhesive fracture, International Journal for Numerical Methods in Engineering 121 (13) (2020) 2946–2963. doi:10.1002/nme.6341.

[32] C. Miehe, F. Aldakheel, A. Raina, Phase field modeling of ductile fracture at finite strains: A variational gradient-extended plasticity-damage theory, International Journal of Plasticity 84 (2016) 1–32. doi:10.1016/j.ijplas.2016.04.011.

[33] M. Ambati, T. Gerasimov, L. De Lorenzis, Phase-field modeling of ductile fracture, Computational Mechanics 55 (5) (2015) 1017–1040. doi:10.1007/s00466-015-1151-4.

[34] R. Alessi, J.-J. Marigo, C. Maurini, S. Vidoli, Coupling damage and plasticity for a phase-field regularisation of brittle, cohesive and ductile fracture: One-dimensional examples, International Journal of Mechanical Sciences 149 (2018) 559–576. doi:10.1016/j.ijmecsci.2017.05.047.

[35] F. Vicentini, J. Heinzmann, P. Carrara, L. De Lorenzis, Variational phase-field modeling of cohesive fracture with flexibly tunable strength surface, Journal of the Mechanics and Physics of Solids 207 (2026) 106424. doi:10.1016/j.jmps.2025.106424.

[36] B. Bourdin, J.-J. Marigo, C. Maurini, C. Zolesi, A variational approach to fracture incorporating any convex strength criterion (Jun. 2025). arXiv:2506.22558, doi:10.48550/arXiv.2506.22558.

[37] C. Miehe, F. Aldakheel, S. Teichtmeister, Phase-field modeling of ductile fracture at finite strains: A robust variational-based numerical implementation of a gradient-extended theory by micromorphic regularization, International Journal for Numerical Methods in Engineering 111 (9) (2017) 816–863. doi:10.1002/nme.5484.

[38] M. Ambati, R. Kruse, L. De Lorenzis, A phase-field model for ductile fracture at finite strains and its experimental verification, Computational Mechanics 57 (1) (2016) 149–167. doi:10.1007/s00466-015-1225-3.

[39] F. Aldakheel, P. Wriggers, C. Miehe, A modified Gurson-type plasticity model at finite strains: Formulation, numerical analysis and phase-field coupling, Computational Mechanics 62 (4) (2018) 815–833. doi:10.1007/s00466-017-1530-0.

[40] I. Ang, N. Bouklas, B. Li, Stabilized formulation for phase-field fracture in nearly incompressible hyperelasticity, International Journal for Numerical Methods in Engineering 123 (19) (2022) 4655–4673. doi:10.1002/nme.7050.

[41] F. Peng, W. Huang, Z.-Q. Zhang, T. Fu Guo, Y. E. Ma, Phase field simulation for fracture behavior of hyperelastic material at large deformation based on edge-based smoothed finite element method, Engineering Fracture Mechanics 238 (2020) 107233. doi:10.1016/j.engfracmech.2020.107233.

[42] L. Zhang, R. Fleischhauer, M. Kaliske, A phase-field fracture model of nearly incompressible hyperelastic material based on a mixed formulation, Proceedings in Applied Mathematics and Mechanics 25 (4) (2025) e70024. doi:10.1002/pamm.70024.

[43] T. K. Mandal, V. P. Nguyen, J.-Y. Wu, A length scale insensitive anisotropic phase field fracture model for hyperelastic composites, International Journal of Mechanical Sciences 188 (2020) 105941. doi:10.1016/j.ijmecsci.2020.105941.

[44] B. Bourdin, G. A. Francfort, J. J. Marigo, Numerical experiments in revisited brittle fracture, Journal of the Mechanics and Physics of Solids 48 (4) (2000) 797–826. doi:10.1016/S0022-5096(99)00028-9.

[45] C. Miehe, F. Welschinger, M. Hofacker, Thermodynamically consistent phase-field models of fracture: Variational principles and multi-field FE implementations, International Journal for Numerical Methods in Engineering 83 (10) (2010) 1273–1311. doi:10.1002/NME.2861.

[46] T. Gerasimov, L. De Lorenzis, On penalization in variational phase-field models of brittle fracture, Computer Methods in Applied Mechanics and Engineering 354 (2019) 990–1026. doi:10.1016/j.cma.2019.05.038.

[47] L. Ambrosio, V. M. Tortorelli, Approximation of functional depending on jumps by elliptic functional via t-convergence, Communications on Pure and Applied Mathematics 43 (8) (1990) 999–1036. doi:10.1002/cpa.3160430805.

[48] I. A. Baratta, J. P. Dean, J. S. Dokken, M. Habera, J. S. Hale, C. N. Richardson, M. E. Rognes, M. W. Scroggs, N. Sime, G. N. Wells, DOLFINx: The next generation FEniCS problem solving environment (Dec. 2023). doi:10.5281/ZENODO.10447666.

[49] S. K. Lam, A. Pitrou, S. Seibert, Numba: A LLVM-based Python JIT compiler, in: Proceedings of the Second Workshop on the LLVM Compiler Infrastructure in HPC, LLVM '15, Association for Computing Machinery, New York, NY, USA, 2015, pp. 1–6. doi:10.1145/2833157.2833162.

[50] S. Timoshenko, Theory of elasticity, third edition. Edition, Engineering societies monographs, McGraw-Hill Education, New Delhi, India, 2010.

Declaration of interests

☒ The authors declare that they have no known competing financial interests or personal relationships that could have appeared to influence the work reported in this paper.

☐ The authors declare the following financial interests/personal relationships which may be considered as potential competing interests: